

Computational modeling of in-stent restenosis

Pharmacokinetic and pharmacodynamic evaluation

Kiran Manjunatha^{a,*}, Nicole Schaaps^c, Marek Behr^b, Felix Vogt^c, Stefanie Reese^a

^a*Institute of Applied Mechanics, RWTH Aachen University*

^b*Chair for Computational Analysis of Technical Systems, RWTH Aachen University*

^c*Department of Cardiology, Pulmonology, Intensive Care and Vascular Medicine, RWTH Aachen University*

Abstract

Persistence of the pathology of in-stent restenosis even with the advent of drug-eluting stents warrants the development of highly resolved *in silico* models. These computational models assist in gaining insights into the transient biochemical and cellular mechanisms involved and thereby optimize the stent implantation parameters. Within this work, an already established fully-coupled Lagrangian finite element framework for modeling the restenotic growth is enhanced with the incorporation of endothelium-mediated effects and pharmacological influences of rapamycin-based drugs embedded in the polymeric layers of the current generation drug-eluting stents. The continuum mechanical description of growth is further justified in the context of thermodynamic consistency. Qualitative inferences are drawn from the model developed herein regarding the efficacy of the level of drug embedment within the struts as well as the release profiles adopted. The framework is then intended to serve as a tool for clinicians to tune the interventional procedures patient-specifically.

Keywords: restenosis, growth factors, smooth muscle cells, endothelium, drug-eluting stents, rapamycin, pharmacokinetics, pharmacodynamics, continuum growth modeling

1. Introduction

In-stent restenosis (ISR) is one of the undesirable outcomes of percutaneous coronary intervention (PCI). It occurs as a result of the damage sustained by the endothelial monolayer as well as the interior layers of the vessel wall during the balloon angioplasty and subsequent stent implantation procedure. It refers to the progressive re-narrowing of the luminal cross-sectional area leading to ischemic events necessitating revascularization but in extreme cases even resulting in myocardial infarction. Despite the randomized trials involving drug-eluting stents (DESs) portraying significant reduction in the occurrence of ISR, due to the complexity of the lesions and of patient-specific characteristics, the real-world registries still show a significant rate of ISR occurrence [1]. In this regard, the growing need for *in silico* tools to predict ISR based on clinical observations has engendered a wide variety of computational models.

*Corresponding author

kiran.manjunatha@rwth-aachen.de

Mies-van-der-Rohe-Str. 1, 52074 Aachen, Germany

1.1. Computational models for ISR

The earliest efforts to model the mechanism of neointimal hyperplasia, the underlying pathological mechanism in ISR, dates back to the work of Evans et al. [2]. They employed coupled cellular automata (CA) and agent-based modeling (ABM) that interact across multiple temporal and spatial scales to describe the multiphysical process of restenosis, which were further resolved by Tahir et al. [3, 4, 5, 6] in terms of capturing the impact of stent design and deployment, functional endothelium, endothelial recovery, and smooth muscle cell migration respectively. Boyle et al. [7, 8] alternatively proposed a hybrid approach wherein a discrete cell-centered-lattice-based approach involving behavioral patterns of cells was assigned to the local environment, while the damage sustained by the arterial wall was quantified using the finite element method (FEM) based on von Mises stresses. Zahedmanesh et al. [9, 10] exploited this hybrid approach to unidirectionally couple FEM and ABM to evaluate and optimize stent deployment parameters including strut thickness and strut spacing. Works of Keshavarzian et al. [11] and Li et al. [12] presented bidirectionally coupled constructs between FEM and ABM, Keshavarzian et al. [11] presenting a general framework for arterial growth and remodeling, while Li et al. [12] specifically focusing on the pathosis of ISR. Nolan and Lally [13] introduced the damage-induced cell proliferative aspects due to both instantaneous and cyclic loading into the coupled FEM and ABM construct. Zun et al. [14] incorporated the blood flow dynamics via FEM and coupled them to an ABM for restenotic growth and presented location-specific validation via comparison to micro-CT and histological data from porcine experiments in Zun et al. [15]. Corti et al. [16] provided a comprehensive overview of pure ABM and the aforementioned hybrid approaches for modeling inflammatory processes in vasculatures.

A separate class of models which rely on a purely continuum-based description of physiological processes involved in ISR has also been proposed. Fereidoon nezhad et al. [17] presented a thermodynamically consistent continuum damage and growth model to model ISR, wherein the multiplicative split in the deformation gradient was employed and an evolution equation for the mass growth resulting in neointima was developed. He et al. [18] then took over the continuum damage and growth model from Fereidoon nezhad et al. [17] and enhanced it with a continuum damage description for the plaque present in the artery before stent implantation. They used this setup to evaluate the quantitative influence of arterial overstretch and overlapping stent struts. In both aforementioned works, damage in the arterial wall was considered to be the main driver for restenotic growth. Escuer et al. [19] presented a highly resolved continuum-based model for ISR, tracking the significant mediators through diffusion-reaction equations and coupling them to a continuum growth description developed by Garikipati et al. [20]. Recently, the authors from our group proposed a fully-coupled Lagrangian FEM framework with coupled advection-reaction-diffusion equations to model the transport of growth mediators linked to a continuum description of growth, incorporating highly resolved chemotactic and haptotactic movements of cellular constituents in [21].

1.2. Computational models comprising pharmacological influence on ISR

The advent of DESs necessitated imbibing the influence of pharmacokinetics and pharmacodynamics associated with the drugs embedded in them to the previously developed ISR models. To the best of the knowledge of the authors, only a handful of models have incorporated the pharmacological effects on restenosis. Caiazzo et al. [22] utilized a lattice Boltzmann flow solver for the blood flow, an ABM for cell dynamics, and a finite difference based drug diffusion scheme to model the multiscale phenomenon of ISR. Rossi et al. [23] on the other hand adopted a continuum description of drug release coupled to the corpuscular approach for neointimal growth presented by Busini et al. [24]. In the recent past, McQueen et al. [25] have presented a comprehensive modeling framework, built on top of the model presented by Escuer et al. [19], incorporating highly resolved drug transport and retention mechanisms demarcating specific and non-specific binding processes. They evaluated the effects of stent design, specifically strut configuration and thickness, and the influence of drug mass and release profiles in the ISR outcome.

Given the scarcity of models in this context, it is the aim of the authors of this work to extend the modeling framework presented by Manjunatha et al. [21] to include endothelium-mediated effects on the process of restenosis in addition to the pharmacological influence of rapamycin-based drugs that are embedded in current generation DESs. The endothelium is modeled as a surface in contrast to the work of Escuer et al. [19], along the lines of the coupled bulk-surface FEM presented in [26]. Damage-induced mechanisms involved in restenosis, which are the key drivers in the works of Escuer et al. [19] and McQueen et al. [25], are foregone. Rather the disruption in the endothelial integrity brought about by stent implantation is considered to be the driver for restenotic growth. Additionally, the stent is not modeled explicitly as done in [19] and [25], but the drug and the pro-inflammatory cytokines are introduced into the system via relevant flux boundary conditions at regions of stent apposition to the arterial wall. Section 2 gives an overview of the pathological mechanisms that are intended to be modeled. Section 3 presents the mathematical model developed, Section 4 includes a short overview of the finite element implementation, Section 5 considers two numerical examples for the evaluation of the capabilities of the model, and finally, Section 6 provides the conclusion and a brief overview of the open questions that have yet to be handled in terms of modeling ISR.

2. Pathophysiological overview

2.1. Endothelium mediated restenotic growth

Vascular endothelia are associated with an array of regulatory functions [27]. They modulate local hemostasis by regulating the release of nitric oxide (NO) and prostacyclin. Apart from both compounds being potent vasodilators, they are also associated with inhibitory effects on platelet activation and aggregation. In addition, endothelial cells (ECs) act as a non-permeable barrier

against blood-flow contents interacting with the subintimal cellular and extracellular constituents. The process of stent implantation strips the vessel wall off its endothelium thereby exposing the extracellular matrix (ECM) and the smooth muscle cells (SMCs) to the blood flow. Fig. 1 portrays the endothelial rupture observed in a stented section of an explanted rat aorta implanted with a XIENCE-V stent. Due to the scarcity of ECs, the production of NO and prostacyclin is hindered, which leads to a reduction in the anti-platelet activity of the remaining ECs. At this stage, platelets and fibrinogen are rapidly deposited at sites of endothelial denudation kickstarting the inflammatory response of the vessel wall involving cytokines, chemokines, and cellular adhesion molecules (CAMs). The deposited platelets get activated and upon degranulation, release platelet-derived growth factor (PDGF) and transforming growth factor (TGF)- β which bring about a proliferative response in the SMCs resulting in neointima formation. Additionally, the upregulated expression of intercellular adhesion molecule (ICAM)-1 and vascular cellular adhesion molecule (VCAM)-1 leads to the recruitment of circulating monocytes at the sites of endothelial injury/dysfunction [28]. These infiltrating monocytes can adhere to the ECM, the stent surface, and/or the fibrin in the thrombus formed after platelet activation [29], and secrete growth factors including PDGF [30, 31], tumor necrosis factor, and several other mediators from the interleukin family. The enhanced presence of PDGF hence brings about an exacerbated proliferation of SMCs resulting in occlusive restenotic growth. In addition, prolonged exposure of the ECs to low/oscillatory shear from the blood flow shall lead to further accumulation of monocytes and low-density lipoproteins in the subintimal space, which can lead to neoatherosclerosis or exaggeration of neointimal hyperplasia.

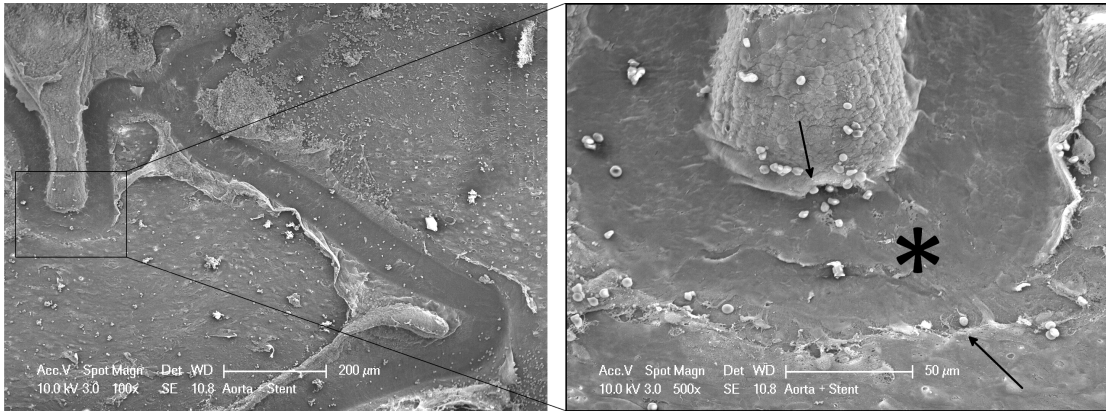


Figure 1: microscopy of an explanted rat aorta (* - ruptured endothelial region)

2.2. Pharmacological influence of rapamycin-based drugs

Rapamycin-based compounds are the most commonly used pharmacological agents that are embedded into modern drug-eluting stents (DESs) and delivered via inorganic polymer layers coated onto the scaffolding stent struts. It is understood that these compounds exert their anti-restenotic effect through two major mechanisms.

1. The drugs bind to what are called the FK506 (tacrolimus)-binding proteins, specifically FKBP12. The complex hence formed then binds to the mammalian target of rapamycin

(mTOR) protein, a signal transduction kinase, hence arresting the progression of the cell cycle, in the case of both SMCs and ECs, beyond the G1 phase [32]. This results in the maintenance of quiescence of the cellular targets, and therefore in the inhibition of their proliferation. Due to this effect acting indiscriminately on both SMCs and ECs, delayed healing of the endothelium is observed after DES implantation, while also suppression of the proliferation of SMCs happens in congruence. In addition, prolonged rapamycin exposure has been shown to reduce the viability of ECs [33], resulting in their apoptosis. Therefore, the usage of rapamycin in DESs engenders effects within the restenotic process which are antithetical.

2. The drug presence in the vessel wall after targeted application via DES is observed via *in vitro* cellular assays to be not sufficient enough to bring about the level of reduction in restenotic growth observed angiographically *in vivo*. It is hence hypothesized that the obscure mechanism that results in significant restenosis reduction is the one attributed to the immunosuppressive nature of rapamycin and its analogs. Systemic application of sirolimus has been shown to reduce the level of EC activation, consequently reducing the expression of ICAM-1 and VCAM-1 [34], which therefore results in a reduced recruitment of monocytes into the subintimal space and their secretion of PDGF. In confluence, these processes result in a significant reduction in restenosis.

To incorporate the previously described EC modulation of the neointimal growth and the pharmacodynamics of rapamycin, the multiphysics modeling framework presented by Manjunatha et al. [21] is extended with two additional field variables, one pertaining to the drug concentration and the other to the EC density. The infiltrating effect of monocytes and their PDGF secretion is indirectly captured by enhancing the source of PDGF through an additional drug-dose-dependent term. Antiproliferative and apoptotic effects of the drug are then coupled back to the platelet aggregation and the inflammatory response. An overview of this updated framework is provided in Fig. 2.

3. Mathematical modeling

To model the pathophysiological and pharmacological processes presented in the previous section, evolution equations are set up for the six mediators of restenosis within the arterial wall and coupled to a continuum growth model. The cellular mediators (SMCs, ECs) of the arterial wall are quantified in terms of cell densities. The extracellular mediators (PDGF, TGF- β and ECM) are quantified in terms of their concentrations. The arterial wall, consistent with the media and the adventitia layers, is modeled as an open system allowing for the transfer of cellular and extracellular species into and out of it. Obviously, the blood flow characteristics in the lumen shall affect the restenotic process as described in the pathophysiology section. However, within the current work, only the possibilities of handling them are discussed but not explicitly considered.

variable type	variable	associated mediator	units
concentration	c_P	PDGF	[mol/mm ³]
	c_T	TGF- β	[mol/mm ³]
	c_C	ECM	[mol/mm ³]
	c_D	drug	[mol/mm ³]
cell density	ρ_S	SMC	[cells/mm ³]
	ρ_E	EC	[cells/mm ²]

Table 1: Transport variables

3.1. Evolution of the mediators of in-stent restenosis

The advection-reaction-diffusion equation forms the basis for modeling the transport phenomena governing the evolution of mediators within the arterial wall. The general form for a scalar field ϕ is given below:

$$\underbrace{\frac{\partial \phi}{\partial t}}_{\text{rate}} \bigg|_{\mathbf{x}} + \underbrace{\text{div}(\phi \mathbf{v})}_{\text{advection}} = \underbrace{\text{div}(k \text{grad} \phi)}_{\text{diffusion}} + \underbrace{\mathcal{R} - \mathcal{S}}_{\text{reaction}}. \quad (1)$$

\mathbf{v} represents the velocity of the medium of transport and k the diffusivity of ϕ in the medium. The above general form is valid for arbitrary points within a continuum body in its current configuration represented by the domain Ω . The terms on the right-hand side of Eq. 1 must now be particularized for the individual mediators. Table 1 lists the variables associated with each mediator and their respective units.

Remark. The cellular and extracellular constituents in the vessel wall undergo constant degradation and regeneration under homeostatic conditions. But within an inflammatory environment (e.g., restenosis, atherosclerosis, fibrosis), this homeostasis is disturbed. For cellular constituents, their programmed death is termed *apoptosis*. Within the context of the mathematical modeling, it is only intended to model the mechanisms involved in the inflammatory processes thereby ignoring the constant degradative and regenerative processes.

3.1.1. Platelet-derived growth factor (PDGF)

PDGF is a key constituent stored within the α -granules of the platelets aggregating at the sites of arterial injury and/or endothelial denudation.

PDGF sources.

In contrast to Manjunatha et al. [21], we herein assume that there are two sources of PDGF. One source (\mathcal{R}_P^1) is through TGF- β (c_T) bringing about autocrine secretion of PDGF by SMCs (ρ_S) [35]. The other (\mathcal{R}_P^2), as mentioned in Section 2, is due to the monocytes infiltrating the subendothelial space as part of the inflammatory response, their differentiation into macrophages, and the ensuing secretion of PDGF [30, 31, 29, 36]. We forego modeling monocyte infiltration with a separate field variable but rather accommodating its effects via TGF- β -induced autocrine secretion. This is reasonable since TGF- β does not contain sources within the arterial wall and its transport can thus be comparable to those of monocytes and differentiated macrophages. A secretion ratio $r_\eta \in [0, 1]$ is introduced in this context, which modulates the relative significance of TGF- β induced PDGF autocrine secretion and the effect of monocyte infiltration. Hence the source term for PDGF reads

$$\mathcal{R}_P := (1 - r_\eta) \mathcal{R}_P^1 + r_\eta \mathcal{R}_P^2, \quad (2)$$

where, as in [21],

$$\mathcal{R}_P^1 := \eta_P \rho_S c_T, \quad (3)$$

where η_P is termed the autocrine PDGF secretion coefficient.

Anti-inflammatory pharmacodynamics.

Further, according to Daniel et al. [34], antiproliferative drugs embedded into DESs, particularly rapamycin-based ones (e.g. sirolimus), induce anti-inflammatory effects in the arterial wall. This leads to a significantly lesser infiltration of monocytes into the subendothelial space, thereby inducing a significant anti-restenotic effect in comparison to the direct inhibition of SMC proliferation by the drug itself. To consider this effect, the latter source term (\mathcal{R}_P^2) is complemented with a factor f_{P1} , which is a function of the drug concentration (c_D), which accounts for the reduction in inflammation due to the drug presence, i.e.,

$$\mathcal{R}_P^2 := f_{P1}(c_D) \eta_P \rho_S c_T. \quad (4)$$

Utilizing Eqs. 3 and 4 in Eq. 2, the source term for PDGF hence reads

$$\mathcal{R}_P := ((1 - r_\eta) + r_\eta f_{P1}(c_D)) \eta_P \rho_S c_T, \quad (5)$$

wherein f_{P1} is chosen to be of the form

$$f_{P1}(c_D) := \exp(-l_{P1} c_D) \in [0, 1], \quad (6)$$

l_{P1} being a parameter that controls the dose-dependent anti-inflammatory effect of the drug (see Fig. 3). This choice is motivated by the fact that rapamycin-based drugs rapidly decrease the expression of cellular adhesion molecules (CAMs) that attract the monocytes into the vessel wall.

The sink term for PDGF is carried over from [21], which is reiterated below for completeness and

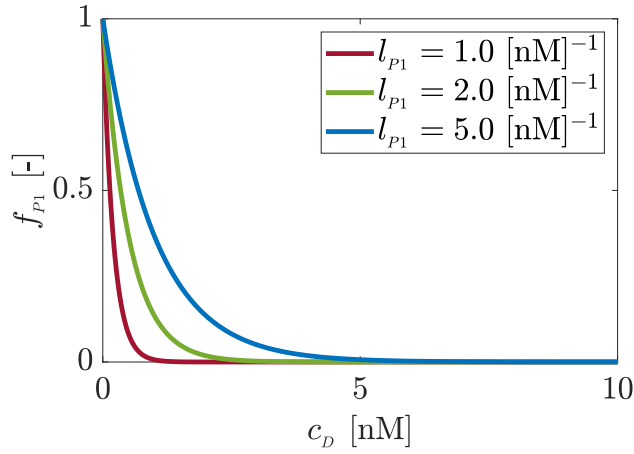


Figure 3: Drug-dependent scaling function for the anti-inflammatory effect

is given by

$$\mathcal{S}_P := \varepsilon_P f_{P2}(c_T) \rho_S c_P, \quad (7)$$

where ε_P is the PDGF receptor internalization coefficient. The sigmoidal function (see [21])

$$f_{P2}(c_T) := \frac{1}{1 + \exp(l_{P2}(c_T - c_{T,th}))} \in [0, 1] \quad (8)$$

captures the scarcity in PDGF receptors induced by TGF- β beyond a certain threshold $c_{T,th}$, and l_{P2} controls steepness of this drop in PDGF receptors.

PDGF is considered freely diffusive in the arterial wall, which is modeled by a standard diffusion term as in Eq. 1. The particularized advection-reaction-diffusion equation for PDGF, by utilizing Eqs. 1, 5 and 7, hence reads

$$\left. \frac{\partial c_P}{\partial t} \right|_{\mathbf{x}} + \text{div}(c_P \mathbf{v}) = \underbrace{\text{div}(D_P \text{grad } c_P)}_{\text{diffusion}} + \underbrace{((1 - r_\eta) + r_\eta f_{P1}(c_D)) \eta_P \rho_S c_T}_{\text{secretion by SMCs and macrophages}} - \underbrace{\varepsilon_P f_{P2}(c_T) \rho_S c_P}_{\text{receptor internalization}}, \quad (9)$$

where D_P refers to the diffusivity of PDGF in the arterial wall.

parameter	description	value	units	ref.
		[media, adventitia]		
D_P	diffusivity	0.1	[mm ² /day]	[37]
r_η	secretion ratio	[0.5, 0.0]	[-]	choice
η_P	autocrine secretion coefficient	1.0×10^{-6}	[mm ³ /cell/day]	choice
l_{P1}	drug-dose-dependent anti-inflammatory parameter	1.0	[nM] ⁻¹	choice
ε_P	receptor internalization coefficient	1.0×10^{-7}	[mm ³ /cell/day]	choice
l_{P2}	steepness coefficient for the drop in PDGF receptors	1.0×10^{16}	[mm ³ /mol]	choice
$c_{T,th}$	TGF- β threshold for the drop in PDGF receptors	1.0×10^{-16}	[mol/mm ³]	choice

Table 2: Model parameters - PDGF

3.1.2. Transforming growth factor (TGF)- β and extracellular matrix (ECM)

Since the equations set up in [21] for the evolution of TGF- β and ECM remain unchanged, we just list them down in their Eulerian forms below, which respectively read

$$\left. \frac{\partial c_T}{\partial t} \right|_{\mathbf{x}} + \operatorname{div}(c_T \mathbf{v}) = \underbrace{\operatorname{div}(D_T \operatorname{grad} c_T)}_{\text{diffusion}} - \underbrace{\varepsilon_T \rho_s c_T}_{\substack{\text{receptor} \\ \text{internalization}}}, \quad (10)$$

$$\left. \frac{\partial c_C}{\partial t} \right|_{\mathbf{x}} + \operatorname{div}(c_C \mathbf{v}) = \underbrace{\eta_C \rho_s \left(1 - \frac{c_C}{c_{C,th}}\right)}_{\substack{\text{secretion by} \\ \text{synthetic SMCs}}} - \underbrace{\varepsilon_C c_P c_C}_{\substack{\text{MMP-induced} \\ \text{degradation}}}, \quad (11)$$

where D_T refers to the diffusivity of TGF- β within the arterial wall, ε_T is termed the TGF- β receptor internalization coefficient, η_C the collagen secretion coefficient, and ε_C the collagen degradation coefficient.

parameter	description	value	units	ref.
TGF-β				
D_T	diffusivity	0.1	[mm ² /day]	[37]
ε_T	receptor internalization coefficient	1.0×10^{-7}	[mm ³ /cell/day]	choice
ECM				
η_C	collagen secretion coefficient	1.0×10^{-8}	[mol/cell/day]	[38]
ε_C	collagen degradation coefficient	1.0×10^{21}	[mm ³ /mol/day]	choice
$c_{C,th}$	collagen secretion threshold	7.0007×10^{-9}	[mol/mm ³]	[39]

Table 3: Model parameters - TGF- β and ECM

3.1.3. Drug

To incorporate the pharmacokinetics, the drug embedded within a polymer layer coated on the metallic core of the DES shall be introduced as an additional mediator c_D into the earlier developed modeling framework. Specifically, rapamycin-based drugs are intended to be investigated. The drug, since it is considered to be eluted from the stent surface, is devoid of any source terms within the arterial wall, rendering

$$\mathcal{R}_D := 0. \quad (12)$$

A sink term takes care of the internalization of targeted receptors for the drug on the SMCs (FKBP12 for rapamycin-based drugs), which results in the deterioration of drug presence. This is formulated as a linear term depending on the local SMC density (ρ_s) and the concentration of the drug itself (c_D), and reads

$$\mathcal{S}_D := \varepsilon_{D1} \rho_s c_D, \quad (13)$$

where ε_{D1} is termed the SMC-pertinent receptor internalisation coefficient for the drug.

The drug is considered freely diffusive in the vessel wall, thereby being modeled by a standard diffusive term. Inserting Eqs. 12 and 13 into the general form in Eq. 1, the balance equation for the drug is then

$$\left. \frac{\partial c_D}{\partial t} \right|_x + \operatorname{div}(c_D \mathbf{v}) = \underbrace{\operatorname{div}(D_D \operatorname{grad} c_D)}_{\text{diffusion}} - \underbrace{\varepsilon_{D1} \rho_S c_D}_{\text{receptor internalization}}, \quad (14)$$

where D_D refers to the drug diffusivity.

One can also embed a more resolved drug transport model to capture the considered drug's receptor-specific and non-specific extracellular binding aspects (see for e.g. [40, 25, 41]) within the current framework with relative ease of implementation.

parameter	description	value	units	ref.
D_D	diffusivity	0.05	[mm ² /day]	[25]
ε_{D1}	SMC receptor internalization coefficient	1.0×10^{-8}	[mm ³ /cell/day]	choice

Table 4: Model parameters - drug

3.1.4. Smooth muscle cells (SMCs)

The modeling of SMCs remains largely unchanged from that in [21], wherein the directional movement of SMCs are modeled via pseudoadvective chemotaxis and haptotaxis velocities given by

$$\begin{aligned} \mathbf{v}_{S1} &:= \chi_{S1} \left(1 - \frac{c_C}{c_{C,th}} \right) \rho_S \operatorname{grad} c_P \\ \mathbf{v}_{S2} &:= -\chi_{S2} f_{S1}(c_P) \rho_S \operatorname{grad} c_C, \end{aligned} \quad (15)$$

wherein χ_{S1} and χ_{S2} denote the respective chemotactic and haptotactic sensitivities of the SMCs, and the sigmoidal scaling factor

$$f_{S1}(c_P) := \frac{1}{1 + \exp(-l_{S1}(c_P - c_{P,th}))} \in [0, 1] \quad (16)$$

controls the switching on of the haptotactic SMC movement beyond a certain threshold of PDGF concentration $c_{P,th}$, l_{S1} modulating the steepness of this switch.

The SMC proliferation assays conducted by Koyama et al. [42] indicate that the SMC proliferation saturates beyond a certain level of PDGF stimulation. In this regard, we forego a linear dependence of the proliferation of SMCs on PDGF concentration (c_P) [21] and introduce a function

$$f_{S2}(c_P) := 1 - \exp(-l_{S2} c_P) \in [0, 1], \quad (17)$$

where l_{S2} is termed the PDGF receptor saturation coefficient.

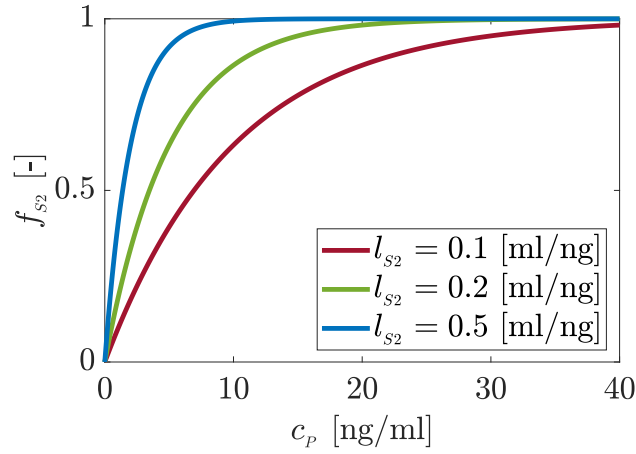


Figure 4: PDGF-dependent SMC proliferation scaling function

The TGF- β induced modulation of SMC proliferation is taken into account as in [21] via a scaling function dependent on the TGF- β concentration (c_T) which is given by

$$f_{s3}(c_T) := \frac{1}{1 + \exp(l_{s3}(c_T - c_{T,th}))} \in [0, 1], \quad (18)$$

where l_{s3} controls steepness of this modulatory effect, and $c_{T,th}$ is the related TGF- β concentration threshold.

To incorporate the direct dose-dependent effect of rapamycin-based drugs on the inhibition of proliferation, an additional drug-dependent scaling function $f_{s4}(c_D)$ has to be introduced. Based on cell proliferation assays conducted by Parry et al. [43], they suggest the Hill type of functions to accommodate the aforementioned effect (sirolimus in this case). We hence incorporate the complimentary curve in our model to scale the proliferativity of SMCs, which reads

$$f_{s4}(c_D) := 1 - \frac{1}{100} \left(\frac{A_s c_D^\alpha}{c_D^\alpha + B_s^\alpha} \right), \quad (19)$$

where A_s is termed the maximum efficacy of the drug in inhibition of SMC proliferation, B_s the drug dose that results in half efficacy, and α the Hill coefficient, B_s and c_D being expressed in [nM] units.

The source term for SMCs is hence arrived at to be of the form

$$\mathcal{R}_s := \eta_s f_{s2}(c_P) f_{s3}(c_T) f_{s4}(c_D) \rho_s \left(1 - \frac{c_C}{c_{C,th}} \right), \quad (20)$$

where η_s is the SMC proliferation coefficient. The constant apoptosis is not intended to be modeled as part of this framework. Hence,

$$\mathcal{S}_s := 0. \quad (21)$$

Using Eqs. 1, 15, 21, and 20, the particularized governing equation for the SMC density is then

arrived at to be

$$\begin{aligned}
\left. \frac{\partial \rho_S}{\partial t} \right|_{\mathbf{x}} + \operatorname{div}(\rho_S \mathbf{v}) = & \underbrace{-\operatorname{div} \left(\rho_S \chi_{S1} \overbrace{\left(1 - \frac{c_C}{c_{C,th}} \right)}^{v_{S1}} \operatorname{grad} c_P \right)}_{\text{chemotaxis}} \\
& + \underbrace{\operatorname{div} \left(\rho_S \chi_{S2} \overbrace{f_{S1}(c_P)}^{-v_{S2}} \operatorname{grad} c_C \right)}_{\text{haptotaxis}} \\
& + \underbrace{\eta_S f_{S2}(c_P) f_{S3}(c_T) f_{S4}(c_D) \rho_S \left(1 - \frac{c_C}{c_{C,th}} \right)}_{\text{proliferation}}.
\end{aligned} \tag{22}$$

parameter	description	value	units	ref.
[media, adventitia]				
χ_{S1}	chemotactic sensitivity	$[1.0 \times 10^{14}, 1.0 \times 10^{13}]$	$[\text{mm}^5/\text{mol}/\text{day}]$	[37]
χ_{S2}	haptotactic sensitivity	$[1.0 \times 10^7, 1.0 \times 10^6]$	$[\text{mm}^5/\text{mol}/\text{day}]$	choice
l_{S1}	steepness coefficient for haptotaxis activation	1.0×10^{16}	$[\text{mm}^3/\text{mol}]$	choice
$c_{P,th}$	PDGF threshold for haptotaxis activation	1.0×10^{-15}	$[\text{mol}/\text{mm}^3]$	choice
η_S	proliferation coefficient	$[0.4, 0.2]$	$[\text{day}]^{-1}$	choice
l_{S2}	PDGF receptor saturation coefficient	1.0×10^{-7}	$[\text{ml}/\text{ng}]$	[42]
l_{S3}	steepness coefficient for TGF- β -induced proliferation modulation	1.0×10^{16}	$[\text{mm}^3/\text{mol}]$	choice
$c_{T,th}$	TGF- β threshold for proliferation inhibition	1.0×10^{-16}	$[\text{mol}/\text{mm}^3]$	choice
A_S	maximum efficacy of the drug against SMC proliferation	69.8	$[\%]$	[43]
B_S	drug concentration for half efficacy	2.2	$[\text{nM}]$	[43]
α	Hill coefficient for drug-induced SMC proliferation inhibition	2.96	$[-]$	[43]

Table 5: Model parameters - SMCs

3.1.5. Endothelial cells (ECs)

The endothelium is a significant mediator for the restenotic process since it moderates the platelet activity as well as the inflammatory response of the arterial wall after stent implantation. The current work intends to incorporate the spatiotemporal effects of stent-induced endothelial denudation and pharmacodynamics-modulated endothelial healing. In this regard, we introduce an additional variable for the EC density ρ_E that resides on the luminal surface only, since the endothelium is a monolayer of ECs.

EC proliferation.

ECs are assumed to proliferate along the endothelium in a logistic fashion. A source term is thereby introduced which looks very similar to the one for ECM secretion in Eq. 11 but with an additional drug-dependent function f_{E1} appended to it, which therefore takes the form

$$\mathcal{R}_E := \eta_E f_{E1}(c_D) \rho_E \left(1 - \frac{\rho_E}{\rho_{E,eq}} \right), \quad (23)$$

where η_E is termed the EC proliferation coefficient, and $\rho_{E,eq}$ is the EC density on a healthy endothelium in homeostasis. For what form of $f_{E1}(c_D)$ to embed, we again turn our attention to a complementary curve to a Hill-type function as in Eq. 19, i.e.,

$$f_{E1}(c_D) := 1 - \frac{1}{100} \left(\frac{A_E c_D^\beta}{c_D^\beta + B_E^\beta} \right), \quad (24)$$

where the constants A_E , B_E , and β can be fit to data (see for e.g. [33]).

EC apoptosis.

Although in a homeostatic environment, apoptosis, which is a highly controlled death of cells in multicellular organisms, is a natural part of the turnover of cellular constituents, in an inflammatory setting, an imbalance persists in the quantitative levels of apoptosis and replenishment of cells. In the case of ECs, this disparity is known to have been exacerbated by the presence of rapamycin-based drugs embedded in DESs [33]. To model this effect, we introduce herein a sink term of the form

$$\mathcal{S}_E := \varepsilon_E f_{E2}(c_D) \rho_E, \quad (25)$$

where ε_E is termed the EC apoptosis coefficient, and $f_{E2}(c_D)$, being termed the drug-dependent apoptosis function chosen to be of the form as in Eq. 17, i.e.,

$$f_{E2}(c_D) := 1 - \exp(-l_E c_D) \in [0, 1]. \quad (26)$$

Here, l_E controls the dose-dependent exacerbation of apoptosis (see Fig. 5).

Remark. The above modeling terms are not sufficient enough to capture the behavior of the ECs, since there shall be no regeneration of the endothelium where the initial value of the EC density (ρ_E) is prescribed to be zero on the assumption of complete denudation ($\mathcal{R}_E = 0$ when $\rho_E = 0$). If one chooses the source term to just be of the form

$$\mathcal{R}_E := \eta_E f_{E1}(c_D) \left(1 - \frac{\rho_E}{\rho_{E,eq}} \right), \quad (27)$$

then, in the absence of the drug, the endothelial recovery happens homogenously throughout the denuded region. This is deemed not to be physiological, and endothelial regeneration is observed to occur from edges inward. To this end, assuming a minuscule amount of diffusivity of ECs shall

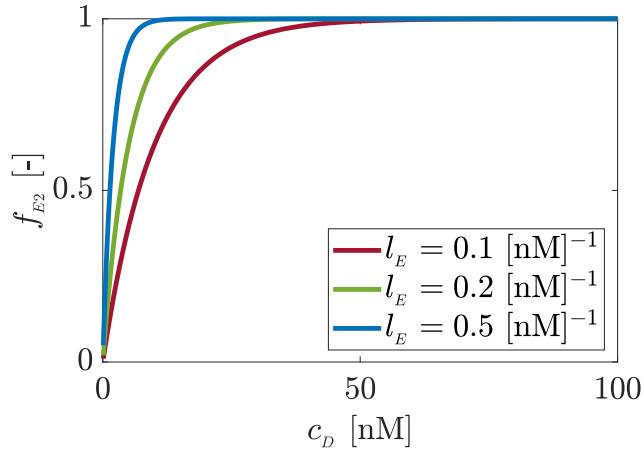


Figure 5: Drug-dependent scaling function for the apoptosis of ECs

enable modeling this process more accurately.

The flow-dependent and chemotactic movements of the ECs are neglected in this work. Considering the ECs to be freely diffusive on the luminal side of the arterial wall, and using Eqs. 1, 23, and 25, the particularized differential equation for the ECs reads

$$\left. \frac{\partial \rho_E}{\partial t} \right|_{\mathbf{x}} + \text{div}_{\Gamma} (\rho_E \mathbf{v}_{\Gamma}) = \underbrace{\text{div}_{\Gamma} (D_E \mathbf{grad}_{\Gamma} \rho_E) + \eta_E f_{E1}(c_D) \rho_E \left(1 - \frac{\rho_E}{\rho_{E,eq}} \right)}_{\text{proliferation}} - \underbrace{\varepsilon_E f_{E2}(c_D) \rho_E}_{\text{apoptosis}} \quad (28)$$

where D_E is the diffusivity of ECs, div_{Γ} and \mathbf{grad}_{Γ} referring to surface divergence and gradient operators respectively.

parameter	description	value	units	ref.
D_E	diffusivity	0.01	[mm ² /day]	choice
η_E	proliferation coefficient	0.1	[day] ⁻¹	choice
$\rho_{E,eq}$	EC density on healthy vascular endothelia	500	[cells/mm ²]	[44]
A_E	maximum efficacy of the drug against EC proliferation	65.4	[%]	[45]
B_E	drug concentration for half efficacy	9.19	[nM]	[45]
β	Hill coefficient for drug-induced EC proliferation inhibition	1.46	[-]	[45]
ε_E	apoptosis coefficient	0.01	[day] ⁻¹	choice
l_E	drug-dose-dependent apoptosis parameter	0.2	[nM] ⁻¹	[33]

Table 6: Model parameters - ECs

3.2. Continuum mechanical modeling

Arterial media and adventitia are considered to be the key layers influencing the structural behavior of the vessel wall, each of which is assumed to be composed of two families of collagen

fibres embedded in an isotropic ground matrix. Proliferativity of the SMCs drives the growth process within the isotropic ground matrix. Collagen, and hence the extracellular matrix, is assumed to modulate the compliance of the arterial wall.

3.2.1. Kinematics

If $\boldsymbol{\varphi}$ is the deformation map between the reference configuration Ω_0 at time t_0 and the current configuration Ω at time t of a continuum body, a particle at position \mathbf{X} in the reference configuration is mapped to that at \mathbf{x} in the current configuration via the deformation gradient $\mathbf{F} = \partial \boldsymbol{\varphi}(\mathbf{X}, t) / \partial \mathbf{X}$. The right and the left Cauchy-Green tensors are further defined by $\mathbf{C} = \mathbf{F}^T \mathbf{F}$ and $\mathbf{B} = \mathbf{F} \mathbf{F}^T$, respectively.

For the description of growth, the well-established multiplicative decomposition of the deformation gradient [46] is adopted, i.e.

$$\mathbf{F} = \mathbf{F}_e \mathbf{F}_g, \quad (29)$$

wherein an incompatible intermediate configuration that achieves a locally stress-free state is achieved via the mapping \mathbf{F}_g , and the elastic deformation gradient \mathbf{F}_e ensures the compatibility of the deformations in the continuum. The elastic right Cauchy-Green tensor and the growth-related right and left Cauchy-Green tensors hence take the forms

$$\begin{aligned} \mathbf{C}_e &:= \mathbf{F}_e^T \mathbf{F}_e = \mathbf{F}_g^{-T} \mathbf{C} \mathbf{F}_g^{-1} \\ \mathbf{C}_g &:= \mathbf{F}_g^T \mathbf{F}_g \\ \mathbf{B}_g &:= \mathbf{F}_g \mathbf{F}_g^T. \end{aligned} \quad (30)$$

3.2.2. Structural tensors

Since the arterial wall is assumed to be composed of collagen fibres arranged in two distinct helices, the notion of structural tensors is introduced in this context to model the initial anisotropic behavior. If \mathbf{a}_{01} and \mathbf{a}_{02} represent the two local collagen orientations in the reference configuration, the associated structural tensors are defined to be

$$\mathbf{H}_1 := \mathbf{a}_{01} \otimes \mathbf{a}_{01}, \quad \mathbf{H}_2 := \mathbf{a}_{02} \otimes \mathbf{a}_{02}. \quad (31)$$

Owing to the symmetry of the above definition, the mapping of the respective structural tensors to the intermediate configuration is achieved by

$$\hat{\mathbf{H}}_i = \mathbf{F}_g \mathbf{H}_i \mathbf{F}_g^T, \quad i = 1, 2, \quad (32)$$

quantities residing in the intermediate configuration being depicted in the form $(\hat{\bullet})$.

3.2.3. Helmholtz free energy

The Helmholtz free energy per unit volume in the reference configuration Ω_0 is split into an isotropic part associated with the isotropic ground matrix, and an anisotropic part corresponding to the collagen fibres. Employing the idea of material isomorphism in the context of inelasticity

[47, 48], the Helmholtz free energy per unit reference volume is defined to be an isotropic function of the selected set of arguments that reside in the stress-free intermediate configuration as

$$\psi := \bar{\psi}(\mathbf{C}_e, \mathbf{B}_g, \hat{\mathbf{H}}_1, \hat{\mathbf{H}}_2, \hat{c}_E). \quad (33)$$

As elucidated in [49], the definition of this stress-free intermediate configuration suffers from the lack of rotational uniqueness. In this context, Holthusen et al. [49] suggest performing a pull-back of the kinematic quantities and the structural tensors defined in Eqs. 30 and 31 to the so-called co-rotated intermediate configuration by using the rotational part $\mathbf{R}_g \in \mathcal{SO}(3)$ of the growth-related deformation gradient $\mathbf{F}_g = \mathbf{R}_g \mathbf{U}_g$, i.e.,

$$\begin{aligned} \bar{\mathbf{C}}_e &:= \mathbf{R}_g^{-1} \mathbf{C}_e \mathbf{R}_g = \mathbf{U}_g^{-1} \mathbf{C} \mathbf{U}_g^{-1} \\ \bar{\mathbf{B}}_g &:= \mathbf{R}_g^{-1} \mathbf{B}_g \mathbf{R}_g \\ \bar{\mathbf{H}}_i &:= \mathbf{R}_g^{-1} \hat{\mathbf{H}}_i \mathbf{R}_g = \mathbf{U}_g \mathbf{H} \mathbf{U}_g. \end{aligned} \quad (34)$$

The volumetric change associated with the deformation gradient \mathbf{F} is deduced to be

$$J = \det \mathbf{F} = \bar{J}_e J_g, \quad \bar{J}_e = \sqrt{\det \mathbf{C}_e}, \quad J_g = \det \mathbf{U}_g. \quad (35)$$

Quantities residing in the aforementioned co-rotated intermediate configuration are depicted in the form $(\bar{\bullet})$. Due to the fact that the Helmholtz free energy is defined to be an isotropic function of its arguments, and that \mathbf{C}_g and \mathbf{B}_g are in possession of the same eigenvalues, and additionally, due to the invariance of the eigenvalues with respect to rotations, the argument \mathbf{B}_g in Eq. 33 can be replaced by \mathbf{C}_g . Hence the referential Helmholtz free energy per unit volume can alternatively be expressed as

$$\psi := \bar{\psi}(\bar{\mathbf{C}}_e, \mathbf{C}_g, \bar{\mathbf{H}}_1, \bar{\mathbf{H}}_2, \bar{c}_C). \quad (36)$$

3.2.4. Clausius-Duhem inequality

The arterial wall and most soft biological tissues are open systems, allowing for heat and mass exchange with the surroundings. In this regard, we consider the isothermal form of the Clausius-Duhem/dissipation inequality suggested by Kuhl and Steinmann [50] for deriving further insights into the growth process which reads

$$-\dot{\psi} + \frac{1}{2} \mathbf{S} : \dot{\mathbf{C}} + \mathcal{R}_0 \geq 0, \quad (37)$$

where \mathbf{S} is the second Piola-Kirchhoff stress tensor, while \mathcal{S}_0 encompasses the entropy sources, sinks, and fluxes that account for biochemical and cellular interactions. The material rate of Helmholtz

free energy hence is given by

$$\dot{\psi} = \dot{\bar{\psi}} = \frac{\partial \bar{\psi}}{\partial \bar{\mathbf{C}}_e} : \dot{\bar{\mathbf{C}}}_e + \frac{\partial \bar{\psi}}{\partial \bar{\mathbf{C}}_g} : \dot{\bar{\mathbf{C}}}_g + \frac{\partial \bar{\psi}}{\partial \bar{\mathbf{H}}_1} : \dot{\bar{\mathbf{H}}}_1 + \frac{\partial \bar{\psi}}{\partial \bar{\mathbf{H}}_2} : \dot{\bar{\mathbf{H}}}_2 + \frac{\partial \bar{\psi}}{\partial \bar{c}_c} : \dot{\bar{c}}_c, \quad (38)$$

with

$$\dot{\bar{\mathbf{C}}}_e = \mathbf{U}_g^{-1} \dot{\mathbf{C}} \mathbf{U}_g^{-1} - \bar{\mathbf{C}}_e \bar{\mathbf{L}}_g - \bar{\mathbf{L}}_g^T \bar{\mathbf{C}}_e, \quad (39)$$

where

$$\bar{\mathbf{L}}_g := \dot{\mathbf{U}}_g \mathbf{U}_g^{-1}. \quad (40)$$

Further, it can be shown that

$$\dot{\bar{\mathbf{C}}}_g = \dot{\mathbf{U}}_g \mathbf{U}_g + \mathbf{U}_g \dot{\mathbf{U}}_g = \bar{\mathbf{L}}_g \bar{\mathbf{C}}_g + \bar{\mathbf{C}}_g \bar{\mathbf{L}}_g^T \quad (41)$$

and

$$\dot{\bar{\mathbf{H}}}_i = \mathbf{U}_g \dot{\mathbf{H}}_i \mathbf{U}_g + \bar{\mathbf{L}}_g \bar{\mathbf{H}}_i + \bar{\mathbf{H}}_i \bar{\mathbf{L}}_g^T, \quad i = 1, 2. \quad (42)$$

In addition, the ECM concentration in the co-rotated intermediate configuration is $\bar{c}_c = J_g^{-1} c_c^0$, which leads to

$$\begin{aligned} \frac{\partial \bar{\psi}}{\partial \bar{c}_c} &= J_g \frac{\partial \bar{\psi}}{\partial c_c^0} \\ \dot{\bar{c}}_c &= J_g^{-1} (\dot{c}_c^0 - c_c^0 \mathbf{I} : \bar{\mathbf{L}}_g) \end{aligned} \quad (43)$$

since $\dot{J}_g = J_g \text{tr}(\bar{\mathbf{L}}_g)$. Plugging Eqs. 39 to 43 into the Clausius-Duhem inequality and employing the Coleman-Noll procedure [51] shall result in the definition of the second Piola-Kirchhoff stress tensor to be

$$\mathbf{S} = 2 \mathbf{U}_g^{-1} \frac{\partial \bar{\psi}}{\partial \bar{\mathbf{C}}_e} \mathbf{U}_g^{-1}. \quad (44)$$

The Clausius-Duhem inequality hence attains the reduced format

$$\mathcal{D}_{\text{red}} := \left[\bar{\mathbf{\Sigma}} - \bar{\mathbf{X}} - \bar{\mathbf{Y}} + c_c^0 \frac{\partial \bar{\psi}}{\partial c_c^0} \mathbf{I} \right] : \bar{\mathbf{L}}_g - \mathbf{G}_1 : \dot{\bar{\mathbf{H}}}_1 - \mathbf{G}_2 : \dot{\bar{\mathbf{H}}}_2 - \frac{\partial \bar{\psi}}{\partial c_c^0} \dot{c}_c^0 + \mathcal{R}_0 \geq 0, \quad (45)$$

where $\bar{\mathbf{\Sigma}}$ and $\bar{\mathbf{X}}$ are the equivalents of the so-called Mandel and back stress tensors, respectively, in the co-rotated intermediate configuration. See Appendix A for the definitions of the other tensors involved in the above expression.

3.2.5. Volumetric growth

It is here that we introduce the definition for the stretch part \mathbf{U}_g of the growth-related deformation gradient \mathbf{U}_g to be of the form prescribed in [21], in line with the suggestion by Lubarda and

Hoger [52] for transversely isotropic growth, i.e.,

$$\mathbf{U}_g := \mathbf{I} + (\vartheta - 1) \boldsymbol{\gamma} \otimes \boldsymbol{\gamma}, \quad (46)$$

where

$$\boldsymbol{\gamma} := \frac{\mathbf{a}_{01} \times \mathbf{a}_{02}}{\|\mathbf{a}_{01} \times \mathbf{a}_{02}\|}. \quad (47)$$

The physical interpretation behind the above definition is that if the growth manifests in a direction orthogonal to the plane consisting of the collagen fibres, the intermediate grown configuration can be deemed stress-free, and so can the previously defined co-rotated intermediate configuration. With the local referential SMC density $\rho_s^0 = J^{-1} \rho_s$ obtained from the balance equation for SMCs (Eq. 22) in hand, and assuming the growth process to arrange the SMCs in such a way that

$$\hat{\rho}_s = \bar{\rho}_s = \rho_{s,eq}, \quad (48)$$

where $\rho_{s,eq}$ refers to the SMC density in a healthy homeostatic artery, we can define the volumetric change associated with growth to be

$$J_g = \vartheta := \frac{\rho_s^0}{\rho_{s,eq}}. \quad (49)$$

Within the context of this work, we forego the concept of remodeling within the arterial wall since in-stent restenosis results from an inflammatory response wherein growth is adjudged to be the dominant effect compared to remodeling. Pathophysiologies including hypertension, fibrosis, aortic aneurysm, etc. warrant considering the remodeling aspects in much detail. Therein, the concept of tensional homeostasis can be exploited [49, 53]. It is therefore assumed that the referential structural tensors \mathbf{H}_1 and \mathbf{H}_2 do not evolve in time rendering $\dot{\mathbf{H}}_1 = \dot{\mathbf{H}}_2 = \mathbf{0}$. The reduced dissipation inequality hence boils down (see Appendix A) to the form

$$\mathcal{D}_{\text{red}} := \left[\bar{\boldsymbol{\Sigma}} - \bar{\mathbf{X}} + c_c^0 \frac{\partial \bar{\psi}}{\partial c_c^0} \mathbf{I} \right] : \bar{\mathbf{L}}_g - \frac{\partial \bar{\psi}}{\partial c_c^0} \dot{c}_c^0 + \mathcal{R}_0 \geq 0. \quad (50)$$

Due to \mathbf{U}_g , and hence $\bar{\mathbf{L}}_g$ (Eq. 40), being prescribed, the expressions for the back stress-like tensor $\bar{\mathbf{X}}$ and the Mandel-like stress tensor $\bar{\boldsymbol{\Sigma}}$ will be an outcome of the dissipation inequality leading to

$$\bar{\boldsymbol{\Sigma}} = \bar{\mathbf{X}} - c_c^0 \frac{\partial \bar{\psi}}{\partial c_c^0} \mathbf{I}, \quad \bar{\mathbf{X}} = 2 \vartheta^2 \frac{\partial \bar{\psi}}{\partial \mathbf{C}_g}, \quad (51)$$

further condensing the dissipation inequality to

$$\mathcal{D}_{\text{red}} := - \frac{\partial \bar{\psi}}{\partial c_c^0} \dot{c}_c^0 + \mathcal{R}_0 \geq 0. \quad (52)$$

The above inequality sheds light on the fact that when $\dot{c}_c^0 \leq 0$, i.e., a degradation in collagen content, it represents a thermodynamically consistent growth process without the entropy source, i.e., $\mathcal{S}_0 = 0$. But when $\dot{c}_c^0 > 0$, which represents secretion of collagen, and hence induction of local

order in the cellular arrangements, the entropy source has to be non-zero locally, specifically,

$$\mathcal{R}_0 \geq \frac{\partial \bar{\psi}}{\partial \bar{c}_c^0} \dot{\bar{c}}_c^0, \quad (53)$$

the arterial wall being an open system allowing for this to be the case.

3.2.6. Choices for the Helmholtz free energies

The specific choice for the non-collagenous isotropic ground matrix, consisting of elastin and SMCs, is assumed to be of the Neo-Hookean form, given by

$$\psi_{iso} = \frac{\mu}{2} (\text{tr } \bar{\mathbf{C}}_e - 3) - \mu \ln \bar{J}_e + \frac{\Lambda}{4} (\bar{J}_e^2 - 1 - 2 \ln \bar{J}_e), \quad (54)$$

where the definition of $\bar{\mathbf{C}}_e$ from Eq. 34, and that of \bar{J}_e from Eq. 35 are utilized. The anisotropic part modeling the behaviour of collagen is particularized to be of exponential form [54] as

$$\psi_{ani} = \frac{k_1}{2k_2} \sum_{i=1,2} (\exp [k_2 \langle \bar{E}_i \rangle^2] - 1), \quad (55)$$

where $\bar{E}_i = \mathbf{H}_i : \bar{\mathbf{C}}_e - 1$, $i = 1, 2$ is the Green-Lagrange strain in the direction of the collagen fibres, and the Macaulay brackets ensure that the fibres are activated only in tension. The stress-like material parameter k_1 in the above definition is here considered to be a linear function of the local ECM concentration in the co-rotated intermediate configuration \bar{c}_E , i.e.,

$$k_1 := \bar{k}_1 \left(\frac{\bar{c}_c}{c_{c,eq}} \right), \quad (56)$$

\bar{k}_1 being the stress-like material parameter for healthy collagen, and $c_{E,eq}$ referring to the homeostatic ECM concentration in a healthy artery. The total Helmholtz free energy per unit referential volume is then the summation

$$\psi = \psi_{iso} + \psi_{ani}. \quad (57)$$

3.2.7. Balance of linear momentum

Since the restenotic process occurs over a period of months, the growth is considered quasistatic, thereby rendering the effects of inertia of the added masses negligible. Hence the quasistatic form of the balance of linear momentum is enforced on the arterial wall, given by

$$\text{Div} (\mathbf{F} \mathbf{S}) + \mathbf{B} = \mathbf{0}, \quad (58)$$

where \mathbf{B} is the body force vector.

parameter	description	value	units	ref.
		[media, adventitia]		
μ	shear modulus for the matrix	[0.02, 0.008]	[M Pa]	[18]
Λ	Lamé parameter for the matrix	10	[M Pa]	[18]
\bar{k}_1	stress-like parameter for collagen fibres	[0.112, 0.362]	[M Pa]	[18]
k_2	exponential coefficient for collagen fibres	[20.61, 7.089]	[-]	[18]
α_a	collagen orientation angle w.r.t circumference	[41, 50.1]	[°]	[18]

Table 7: Model parameters - structural

3.3. Boundary conditions

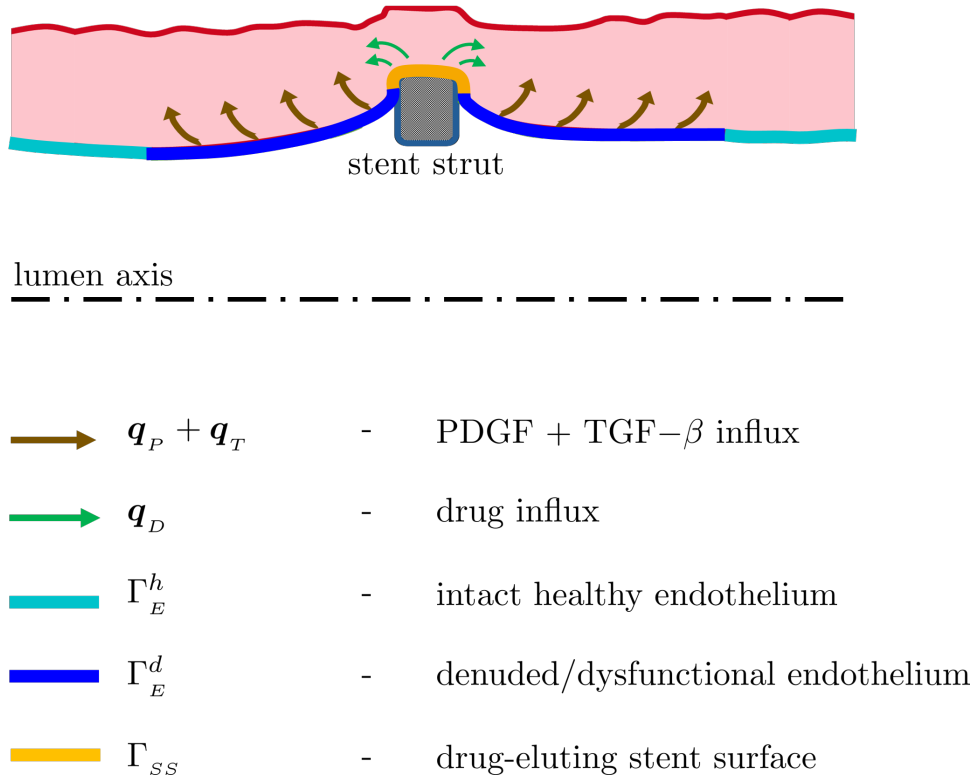


Figure 6: Boundary conditions

All the relevant boundary conditions are summarized in Table 8. The whole boundary of the arterial wall Γ is first divided into the boundary exposed to the lumen Γ_l , and the remaining boundary Γ_r , i.e., $\Gamma = \Gamma_l \cup \Gamma_r$. Further, Γ_l is partitioned into the endothelium Γ_E and drug-eluting stent surface Γ_{SS} , i.e., $\Gamma_l = \Gamma_E \cup \Gamma_{SS}$. Finally, the endothelium Γ_E is subdivided into the transient boundaries which represent the intact healthy endothelium (Γ_E^h) and the denuded/dysfunctional endothelium (Γ_E^d) respectively, i.e., $\Gamma_E = \Gamma_E^h \cup \Gamma_E^d$. The boundaries lining the endothelium are just denoted $\partial\Gamma_E$.

- (a) Through the process of platelet aggregation, activation, and degranulation, PDGF and TGF- β enter the arterial wall at sites of endothelial damage exacted by stent implantation as well as

	variable	Dirichlet	region	Neumann	region
(a)	c_P	—	—	$\mathbf{q}_P \cdot \mathbf{n} = \bar{q}_P := f_{B1}(t) \left(1 - \frac{\rho_E}{\rho_{E,eq}}\right) \bar{q}_P^{\text{ref}}$	$\forall \mathbf{x} \in \Gamma_E$
				$\text{grad}(c_P) \cdot \mathbf{n} = 0$	$\forall \mathbf{x} \in \Gamma \setminus \Gamma_E$
	c_T	—	—	$\mathbf{q}_T \cdot \mathbf{n} = \bar{q}_T := f_{B1}(t) \left(1 - \frac{\rho_E}{\rho_{E,eq}}\right) \bar{q}_T^{\text{ref}}$	$\forall \mathbf{x} \in \Gamma_E$
				$\text{grad}(c_T) \cdot \mathbf{n} = 0$	$\forall \mathbf{x} \in \Gamma \setminus \Gamma_E$
(b)	c_D	—	—	$\mathbf{q}_{D1} \cdot \mathbf{n} = \bar{q}_{D1} := f_{B2}(t) \bar{q}_D^{\text{ref}}$	$\forall \mathbf{x} \in \Gamma_{SS}$
				$\mathbf{q}_{D2} \cdot \mathbf{n} = \bar{q}_{D2} := -\varepsilon_{D2} \rho_E c_D$	$\forall \mathbf{x} \in \Gamma_E$
				$\text{grad}(c_D) \cdot \mathbf{n} = 0$	$\forall \mathbf{x} \in \Gamma \setminus (\Gamma_{SS} \cup \Gamma_E)$
(c)	c_C	—	—	$\text{grad}(c_C) \cdot \mathbf{n} = 0$	$\forall \mathbf{x} \in \Gamma$
	ρ_S	—	—	$\text{grad}(\rho_S) \cdot \mathbf{n} = 0$	$\forall \mathbf{x} \in \Gamma$
	ρ_E	—	—	$\text{grad}(\rho_E) \cdot \mathbf{n} = 0$	$\forall \mathbf{x} \in \partial\Gamma_E$
(d)	\mathbf{u}	$\mathbf{u} = \bar{\mathbf{u}}$	$\forall \mathbf{x} \in \Gamma_{0,u}$	$\mathbf{T} = \mathbf{P} \cdot \mathbf{N} = \bar{\mathbf{T}}$	$\forall \mathbf{x} \in \Gamma_{0,T}$

Table 8: Boundary conditions

at sites of dysfunctional endothelial barrier function induced by the blood flow dynamics and the pharmacodynamics (Γ_E in Fig. 6). PDGF and TGF- β hence shall have their respective influxes prescribed in the form

$$\begin{aligned}
\mathbf{q}_P \cdot \mathbf{n} &= \bar{q}_P := f_{B1}(t) \left(1 - \frac{\rho_E}{\rho_{E,eq}}\right) \bar{q}_P^{\text{ref}} \\
\mathbf{q}_T \cdot \mathbf{n} &= \bar{q}_T := f_{B1}(t) \left(1 - \frac{\rho_E}{\rho_{E,eq}}\right) \bar{q}_T^{\text{ref}} \quad \forall \mathbf{x} \in \Gamma_E
\end{aligned} \tag{59}$$

where \bar{q}_P^{ref} and \bar{q}_T^{ref} are parameters controlling the peaks of the respective influx profiles. f_{B1} is a time (t)-dependent scaling function defined as

$$f_{B1}(t) := 1 - \exp(-l_B t) \tag{60}$$

where the parameter l_B modulates the slope of the influx profiles, thereby indirectly prescribing the time required to reach the peak influxes \bar{q}_P^{ref} and \bar{q}_T^{ref} , and $f_{B1}(t)$ behaves qualitatively similar to $f_{E2}(c_D)$ (see Fig. 5). The dependence of both \bar{q}_P and \bar{q}_T on the EC density (ρ_E) is prescribed so as to render the influx of growth factors dependent on the health of the endothelium. The larger the deviation from the homeostatic value of EC density ($\rho_{E,eq}$), the more the dysfunctional behavior of the endothelium, allowing for more platelet aggregation and influx of PDGF and TGF- β , and enhanced monocyte infiltration. Homogeneous Neumann

boundary conditions are applied on the remaining boundaries.

- (b) Drug from the DES is assumed to directly diffuse into the vessel wall regions of stent apposition against the vessel wall. Hence an influx of the drug is prescribed on the aforementioned contact surface (Γ_{ss} in Fig. 6) in the form

$$\mathbf{q}_{D1} \cdot \mathbf{n} = \bar{q}_{D1} := f_{B2}(t) \bar{q}_D^{\text{ref}}, \quad (61)$$

where q_D^{ref} is a parameter controlling the peak of the influx profile, while f_{B2} is a time (t)-dependent factor defined to be

$$f_{B2}(t) := \exp\left(-\frac{t}{f_{B3}(t_c)}\right) \left(1 - \exp\left(-\frac{t}{t_c}\right)\right), \quad (62)$$

wherein

$$f_{B3}(t_c) := t_2 \exp\left(\frac{t_p}{t_c}\right) - t_c. \quad (63)$$

Here, t_p and t_c are time-like parameters that control the curvature of the influx profile, and t_p can be interpreted to be the time to achieve peak influx of the drug. Exemplary drug influx profiles and the associated cumulative drug release profiles are shown in Fig. 7.

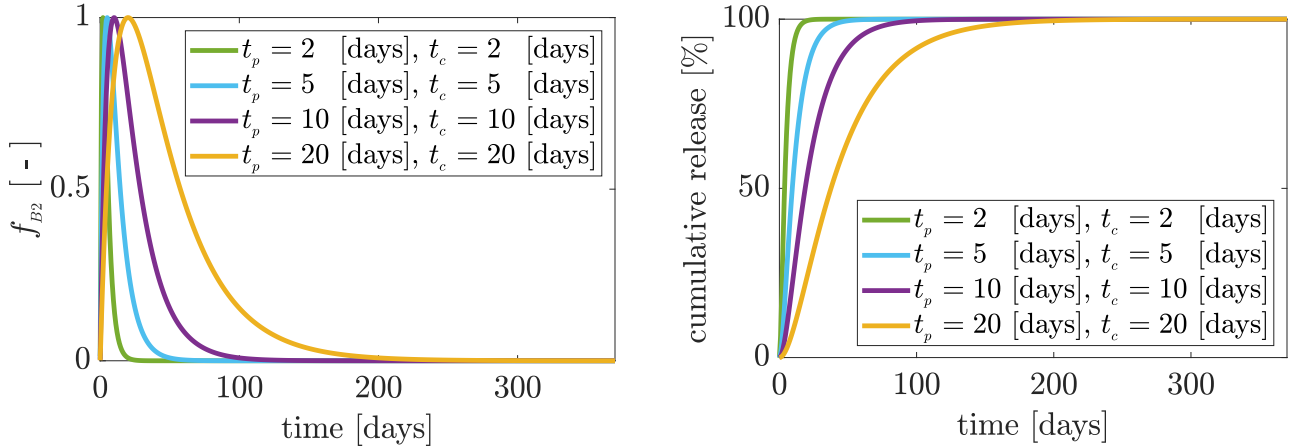


Figure 7: left - drug influx profiles; right - cumulative release profiles

The binding of the drug to the FKBP12 receptors on the ECs is modeled via a flux boundary condition on the luminal surface of the form

$$\mathbf{q}_{D2} \cdot \mathbf{n} = \bar{q}_{D2} := -\varepsilon_{D2} \rho_E c_D, \quad (64)$$

ε_{D2} being termed the EC-pertinent receptor internalization coefficient for the drug. Homogeneous Neumann boundary conditions are applied on the remaining boundaries.

- (c) ECM (c_E), SMCs (ρ_s) and ECs (ρ_{en}) are all considered constrained within the arterial wall. Therefore homogeneous Neumann boundary conditions are prescribed for the respective balance equations on the entire boundary of the vessel wall.

- (d) Displacements are prescribed on the boundary $\Gamma_{0,u}$ in the reference configuration, and tractions on the boundary $\Gamma_{0,T}$ in the reference configuration. Also, the total boundary in the reference configuration $\Gamma_0 = \Gamma_{0,u} \cup \Gamma_{0,T}$.

3.4. Initial conditions

The initial ECM concentration (c_C) and SMC density (ρ_S) are prescribed to be those of a healthy homeostatic artery in equilibrium in the entire domain of the arterial wall. PDGF, TGF- β , and the drug are considered initially absent in the vessel wall. EC density (ρ_E) is prescribed to be zero at regions where endothelial denudation is observed/expected (Γ_E^d), and to be that on a healthy homeostatic artery in equilibrium ($\rho_{E,eq}$) elsewhere (Γ_E^h). Table 9 summarizes the relevant initial conditions.

variable	initial condition	region
c_P	0	$\forall \mathbf{x} \in \Omega$
c_T	0	$\forall \mathbf{x} \in \Omega$
c_C	c_C	$\forall \mathbf{x} \in \Omega$
c_D	0	$\forall \mathbf{x} \in \Omega$
ρ_S	$\rho_{S,eq}$	$\forall \mathbf{x} \in \Omega$
ρ_E	0	$\forall \mathbf{x} \in \Gamma_E^d$
ρ_E	$\rho_{E,eq}$	$\forall \mathbf{x} \in \Gamma_E^h$

Table 9: Initial conditions

4. Finite element implementation

The coupled differential equations, i.e., Eqs. 9, 10, 11, 14, and 22, are first transformed to their Lagrangian equivalents as done by Manjunatha et al. [21]. All the balance equations, except that of the EC density (ρ_E), in their weak forms, are solved in the arterial wall domain, spatially discretized by trilinear hexahedral elements. The EC density (ρ_E) field is solved for on the lumen surface, spatially discretized using bilinear quadrilaterals projected from the bulk arterial wall mesh. This projected surface mesh is also utilized in prescribing flux (inhomogeneous Neumann) boundary conditions. Temporal discretization is performed utilizing the fully-implicit backward-Euler method. Additionally, for the SMC density (ρ_S) field, the streamline-upwind Petrov-Galerkin (SUPG) method is incorporated in order to ensure robust finite element computations at high chemotactic and haptotactic velocities of the SMCs. The system matrices intertwine with each other at the common nodes shared between the bulk hexahedrons and the surface quadrilaterals. The framework presented is implemented into the commercial finite element program FEAP

via its user-defined element interface. The tangential stiffness matrices involved in each global Newton iteration of the nonlinear problem are obtained via algorithmic differentiation using the *Wolfram Mathematica* package *AceGen* [55, 56]. The solution of the linear system of equations in every global Newton iteration is efficiently accomplished with the help of the parallelized PARDISO solver [57, 58, 59] through a user-defined macro.

5. Numerical evaluation

To evaluate the computational model presented herein, two boundary value problems (BVPs) are set up. The first BVP presents a simplified representation of a stented arterial quadrant with partial endothelial denudation, utilizing which the spatiotemporal evolution of the mediators of restenosis are examined. Additionally, the respective influences of the severity in the inflammatory response post stenting as well as the level of drug embedment in the stent struts are evaluated. Following this, a longitudinal section of a coronary artery implanted with the XIENCE-V stent is considered for the numerical evaluation. In both the BVPs, media and adventitia are considered to constitute the bulk of the arterial wall, while the endothelium is modeled as a surface on the luminal side. Arterial overstretch is ignored in this context since the denudation of the endothelium is considered the key driver for the restenotic process.

5.1. Simplified stented arterial segment

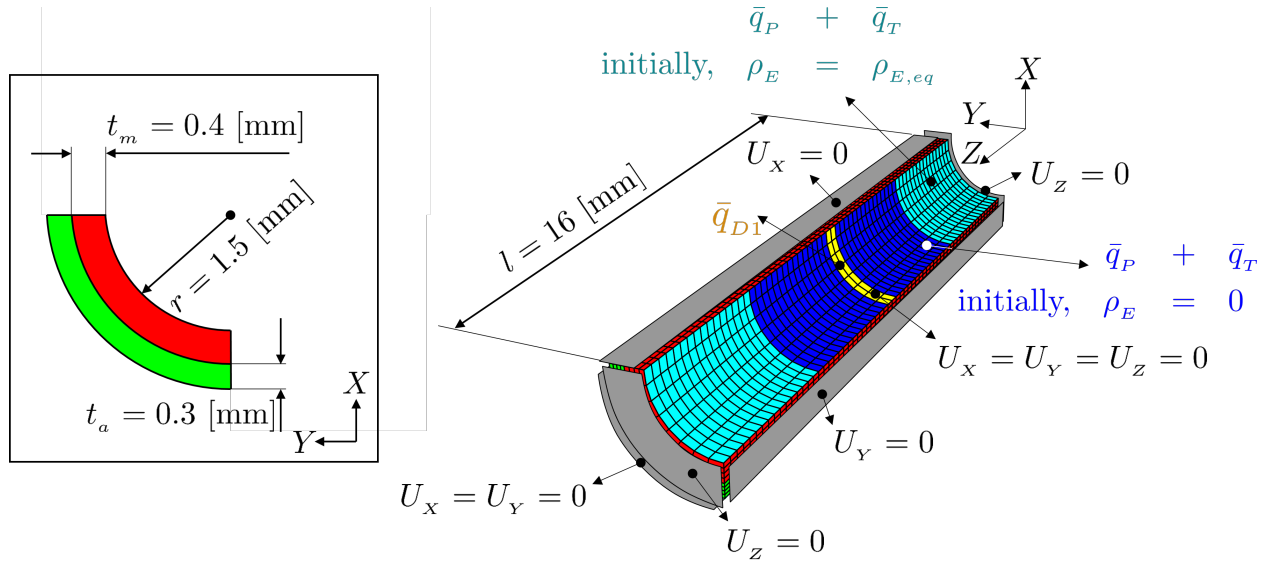


Figure 8: Simplified stented arterial segment

A quadrant of an artery of length $l = 16$ [mm], lumen radius $r = 1.5$ [mm], medial thickness $t_m = 0.4$ [mm], and adventitial thickness $t_a = 0.3$ [mm] is constructed as shown in Fig. 8. A segment of length 0.5 [mm] on the luminal surface of the arterial wall at mid-length ($Z = 8$ [mm]) is considered to be the region of stent apposition (Γ_{ss}). Regions of length 3.5 [mm] on each side of

the stent apposition are considered denuded of endothelial cells (Γ_E^d). The rest of the inner surface of the vessel wall is considered to possess a healthy endothelium (Γ_E^h).

5.1.1. Discretization

The geometry is spatially discretized with trilinear hexahedral elements, 64 of them along the longitudinal direction, 8 along the circumference, and 4 along the radial direction of each layer of the arterial wall. Projected surface meshes on the luminal side represent the stent apposition region as well as the denuded and healthy endothelial regions. The problem is temporally discretized with a time-step Δt of 1 [days].

5.1.2. Boundary and initial conditions

Displacement boundary conditions mimicking the symmetry of the arterial wall are prescribed. The ends are fixed against longitudinal movement. The abluminal side of the vessel wall is constrained against displacements in the circumferential and radial directions. The boundary and initial conditions are prescribed as elucidated in Section 3.3 on respectively annotated regions in Fig. 8.

5.1.3. Parameters

Out of the 39 parameters listed in Tables 2 to 6, 20 are carried over from relevant literature. The remaining 19 are chosen in such a way that the transient response of the mediators and the macroscopic outcome is physiological.

5.1.4. Results and discussion

Three aspects of pharmacokinetics and pharmacodynamics are evaluated using the simplified model setup.

1. The level of drug embedment in the stent strut, controlled via the drug influx parameter \bar{q}_D^{ref}
2. Drug release rate prescribed by the release profiles depicted in Fig. 7
3. Severity of patient-specific inflammatory response, controlled by the PDGF secretion ratio r_η

Influence of the level of drug embedment in the stent strut.

Fig. 9 portrays how at point P the evolution of the growth stretch $\vartheta = J_g$ and the mediators of the restenotic growth is influenced by \bar{q}_D^{ref} for a fixed release profile and a PDGF secretion ratio of $r_\eta = 0.5$. It is interesting to note that a nonlinear behavior is observed in the growth evolution for increasing levels of drug embedment. For this particular BVP and the choice of parameters, $\bar{q}_D^{\text{ref}} = 10$ [fmol/mm²/day] is determined to be the optimal peak drug influx across the stent contact surface. Beyond this, the apoptotic and antiproliferative mechanisms induced in the ECs due to the drug become predominant, thereby slowing down the healing of the endothelium and allowing for more platelet degranulation and monocyte infiltration into the subendothelial space. The delay in endothelial healing is clearly observable in the evolution of ρ_E . This result is in contradiction to the investigation presented by McQueen et al. [25], wherein the restenotic growth was observed to be

monotonically decreasing and reaching an asymptotic limit beyond which there was no observable difference in thickness of the neointimal tissue. Although the authors therein consider a highly resolved drug transport and SMC proliferation model, due to the neglect of pharmacodynamic effects on ECs in their model, this disparity is justified.

Influence of the drug release profile.

Restenotic growth is investigated for two levels of drug embedment and varying drug release profiles (see Fig. 7), and the resulting neointima profiles are plotted in Fig. 11. At low levels of drug mass embedded in the stent strut, a slow release of the drug into the arterial wall results in the least neointimal growth. But at the optimal drug embedment associated with $\bar{q}_D^{\text{ref}} = 10$ [fmol/mm²/day], the influence of the release profiles is negligible. However, a non-monotonic behavior is observed, as can be seen in the magnified images. This non-monotonicity is also what McQueen et al. [25] discerned in their investigations but the trend was consistent across all drug masses in their work, whereas a shift is observed herein.

Influence of severity of the inflammatory response.

The inflammatory response, specifically the expression of cell adhesion molecules (ICAM-1 and VCAM-1) on the endothelial surface, highly influences the pharmacodynamics [34] since they alter the amount of infiltrating monocytes, and consequently, the amount of PDGF sourced within the vessel wall. This effect is clearly seen in Fig. 11 where the neointima profiles for two different values of r_η are presented for varying drug embedment levels. The optimal range of the embedded drug mass becomes wider and more effective at high values of r_η since the anti-inflammatory effects of the drug become highly influential. In all cases, an increased drug presence beyond an optimal range shall drastically enhance the inflammation and thereby the restenotic growth, almost equivalent to levels observed after BMS implantation.

5.2. Coronary artery implanted with XIENCE-V stent

A segment of the human coronary artery of length $l = 2.32$ [mm], implanted with the XIENCE-V stent, is constructed using the stent geometry as shown in the top in Fig. 12. This segment is chosen since it repeats itself longitudinally throughout the length of the stent.

5.2.1. Discretization

The geometry of the arterial wall is spatially discretized with 99,368 trilinear hexahedral elements in the bulk, 4 elements along the thickness of each layer. The stent apposition surface, projected from the bulk, contains 2054 bilinear quadrilateral elements. The rest of the luminal surface then consists of 10,367 bilinear quadrilaterals. Temporal discretization is again in terms of $\Delta t = 1$ [days].

5.2.2. Boundary and initial conditions

The stented surface is constrained against all displacements, while the exterior surface of the geometry is constrained against movements in circumferential and radial directions as is the case in

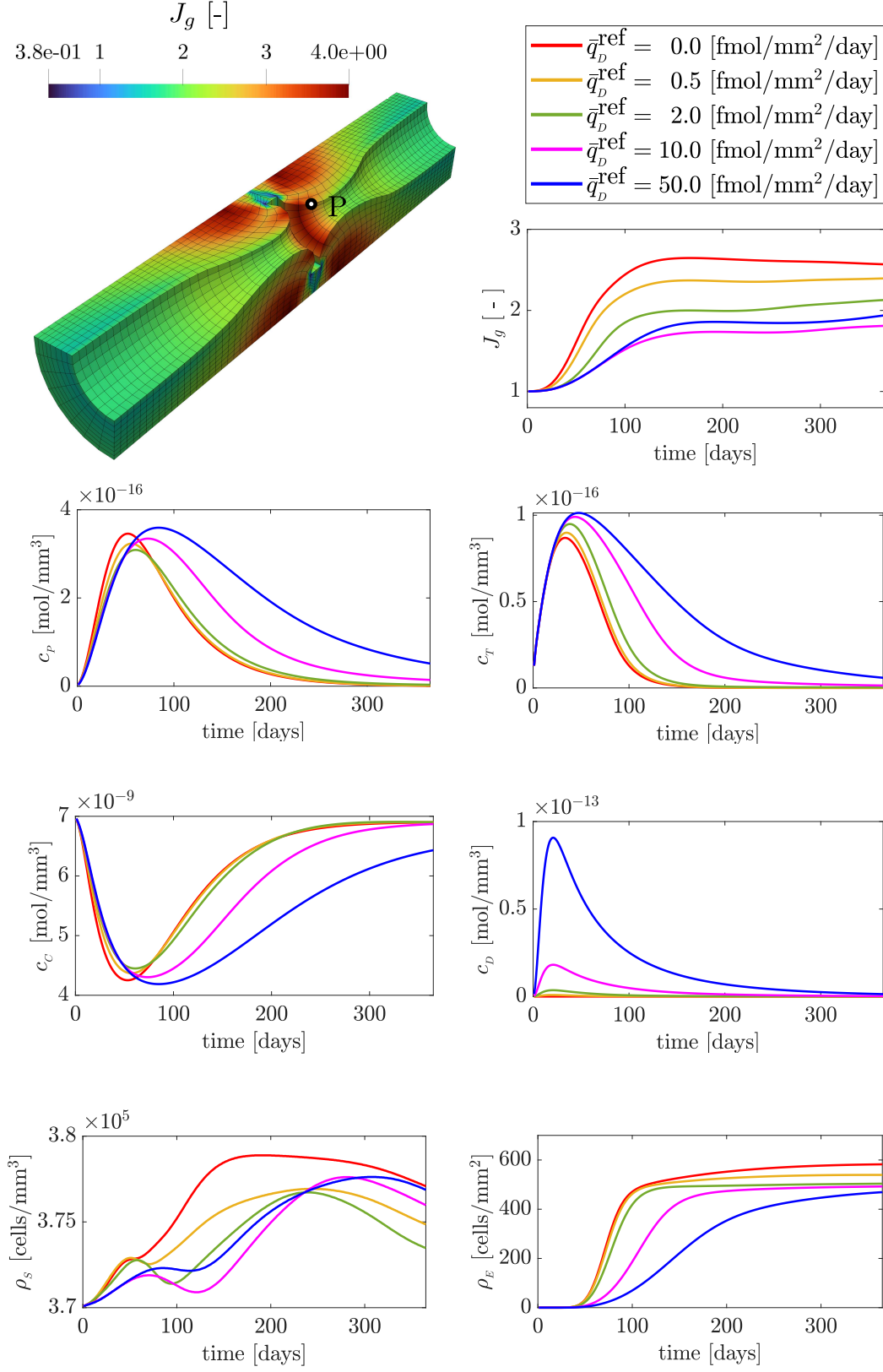


Figure 9: Evolution of quantities of interest at point P

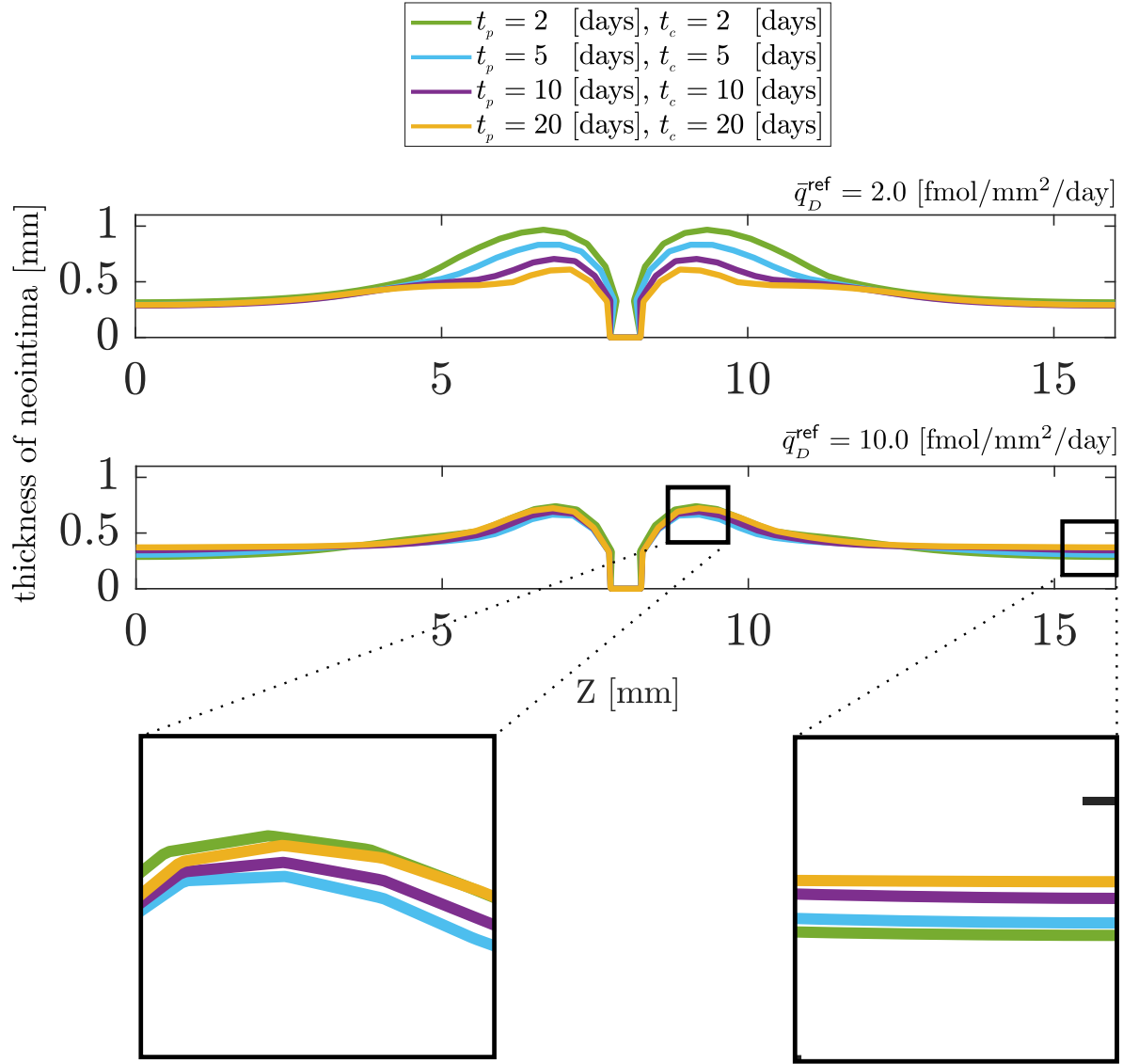


Figure 10: Neointima profiles for varying drug influx profiles (see Fig. 7)

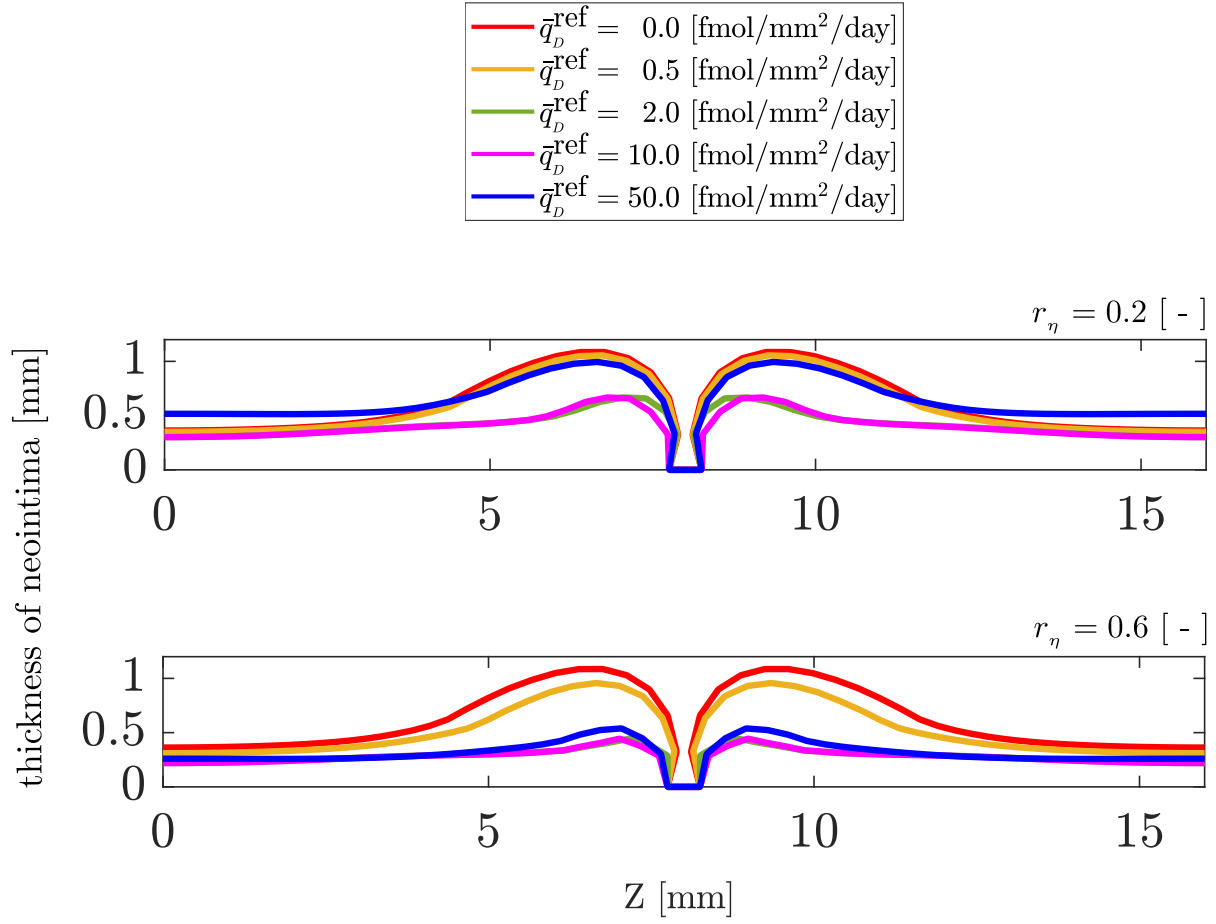


Figure 11: Neointima profiles for varying PDGF secretion ratios

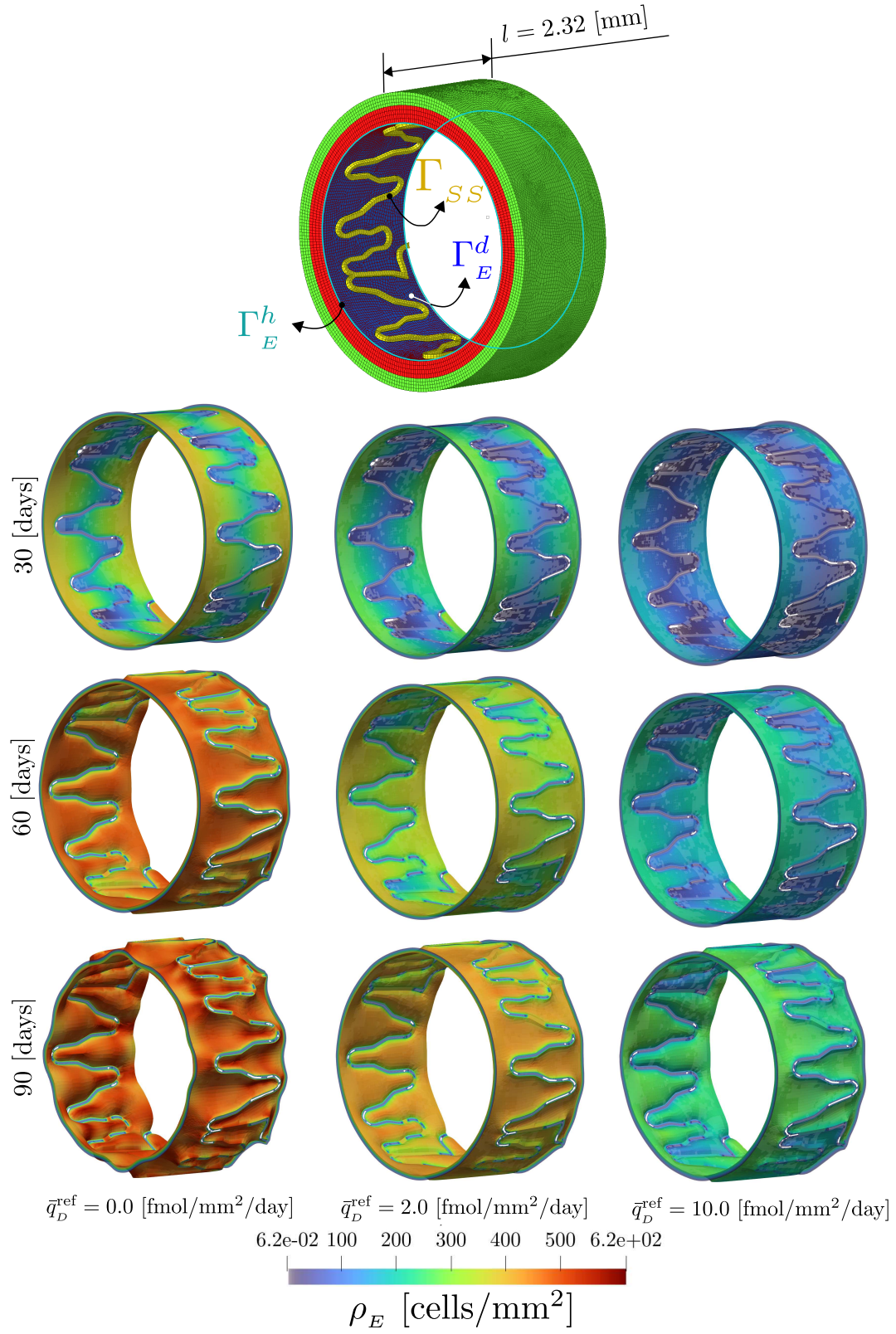


Figure 12: Evolution of endothelial health

Section 5.1. The color coding for the discretized representation at the top of Fig. 12 is maintained to be the same as in Fig. 8 to emphasize the fact that all flux boundary conditions are applied exactly as in Section 5.1 on the corresponding boundary domains. The only difference lies in the prescription of the initial values of EC density (ρ_E). While the entire luminal surface is considered denuded, to initiate the healing of the endothelium, the values for ρ_E are prescribed initially to be $\rho_{E,eq}$ along the annular edges at the longitudinal ends of the surface, and it is set to be zero elsewhere.

5.2.3. Parameters

The model parameters remain the same as in the previous numerical example.

5.2.4. Results and discussion

A period of 90 [days] after stent implantation was simulated using the BVP setup. This is due to the fact that stent strut coverage by neointimal is not modeled as part of the presented methodology. In this regard, the obstruction of the stent apposition against restenotic growth is artificial. The results hence serve only as a reflection of the capability of the model to capture the intricate pathophysiology within complex geometric settings.

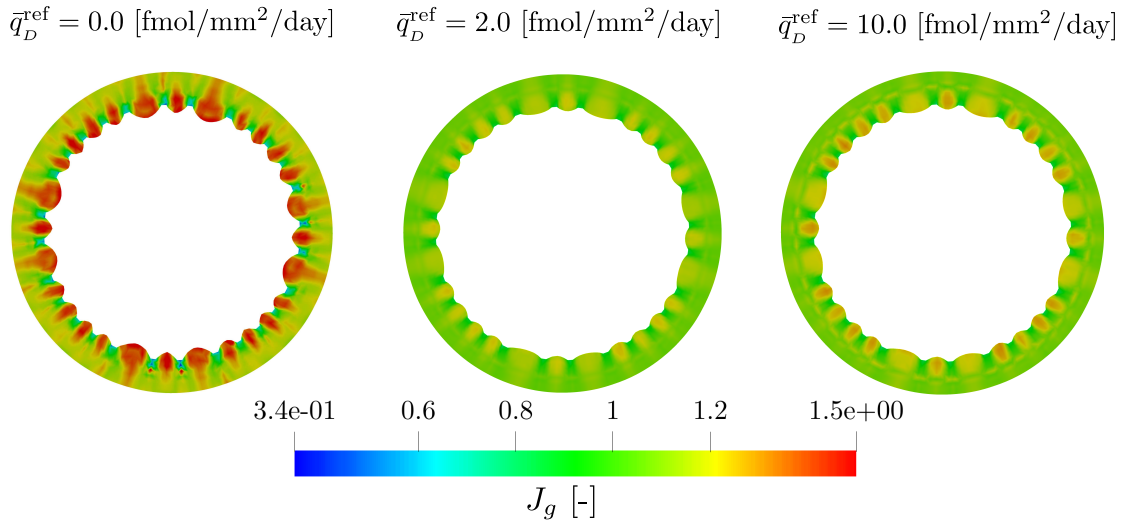


Figure 13: Mid-length slices of growth stretch at 90 [days]

The collage in Fig. 12 presents the transient process of endothelial healing through 90 [days] for different levels of drug embedment. As expected, the restenotic growth is much pronounced in the case of bare metal stent struts, while also the endothelial recovery is relatively faster compared to DES. Additionally, drug mass optimality is observed at $\bar{q}_D^{\text{ref}} = 2.0 \text{ [fmol/mm}^2\text{/day]}$ beyond which there is an increase in neointimal growth. This is clearly demonstrated in Fig. 13 where mid-length slices (at $l = 1.16 \text{ [mm]}$) representing the growth stretch J_g are plotted.

6. Conclusion and outlook

The current work presents a computational modeling framework to model the spatiotemporal evolution of neointimal growth observed during the pathophysiology of in-stent restenosis. The main contribution of the work lies in capturing the regulatory effects of the endothelium in stented sections of arteries, endothelial recovery, and the pharmacological influence of rapamycin-based drugs on the very intricate restenotic process. The transient evolutions of the significant mediators, including the ECs and the drug, are then coupled to a transversely isotropic constitutive description of the arterial wall through thermodynamically consistent growth kinematics. The framework can model the complex interplay between the mediators, providing significant resolution into cellular and biochemical interactions. Through the numerical investigations, it has been demonstrated that there is scope for optimization of the drug content embedded within the struts of DESs as well as the drug release profiles adopted. Finally, the influence of the patient-specific immunological response that governs the severity of the inflammatory response is observed to bear a significant influence on the aforementioned optimization.

It is to be noted that the model presented considers the denudation of endothelium to be the only driver of restenotic growth. While it does play a significant role, it is not the only source of neointimal hyperplasia. The arterial overstretch is diagnostically determined to be the other important aspect that has to be considered in the modeling approach. In this context, implementing a damage-dependent multiphysical model developed by Gierig et al. [60] shall render a significantly enhanced resolution to the computational model. The other crucial aspect that has to be dealt with is the effect of blood dynamics, particularly the arterial wall shear stress, and pharmacokinetics of the drug that leads to downstream deposition owing to the lipophilic nature of the drug. Embedding the hence fully resolved multiphysics-based model within a fluid-structure interaction (FSI) framework shall then enable accurate patient-specific risk prediction and pharmacological evaluation.

The predicament lies in validating the complex computational model through suitable experiments. Although several of the modeling parameters are extracted from literature which presents immunohistochemical assays, the rest of them have been chosen based on physiological insights and expected outcomes. The computational model hence serves as a tool to pick possible avenues for experimental validation, the identification of which is based currently either on physiological intuition or extensive data analytics.

Appendices

Appendix A. Clausius-Duhem inequality

Using Eqs. 38, 39, 41, and 42 in the Clausius-Duhem inequality (Eq. 37), we arrive at the reduced dissipation inequality in the form

$$\begin{aligned} \mathcal{D}_{\text{red}} &:= \left(2\bar{\mathbf{C}}_e \frac{\partial \bar{\psi}}{\partial \bar{\mathbf{C}}_e} - 2 \frac{\partial \bar{\psi}}{\partial \mathbf{C}_g} \mathbf{C}_g - 2 \frac{\partial \bar{\psi}}{\partial \bar{\mathbf{H}}_1} \bar{\mathbf{H}}_1 - 2 \frac{\partial \bar{\psi}}{\partial \bar{\mathbf{H}}_2} \bar{\mathbf{H}}_2 + c_c^0 \frac{\partial \bar{\psi}}{\partial c_c^0} \mathbf{I} \right) : \bar{\mathbf{L}}_g \\ &\quad - \left(\mathbf{U}_g \frac{\partial \bar{\psi}}{\partial \bar{\mathbf{H}}_1} \mathbf{U}_g \right) : \dot{\mathbf{H}}_1 - \left(\mathbf{U}_g \frac{\partial \bar{\psi}}{\partial \bar{\mathbf{H}}_2} \mathbf{U}_g \right) : \dot{\mathbf{H}}_2 \\ &\quad - \frac{\partial \bar{\psi}}{\partial c_c^0} \dot{c}_c^0 + \mathcal{R}_0 \geq 0. \end{aligned} \tag{A.1}$$

Introducing the following definitions as in Holthusen et al. [49],

$$\begin{aligned} \bar{\Sigma} &:= 2\bar{\mathbf{C}}_e \frac{\partial \bar{\psi}}{\partial \bar{\mathbf{C}}_e} \\ \bar{\mathbf{X}} &:= 2 \frac{\partial \bar{\psi}}{\partial \mathbf{C}_g} \mathbf{C}_g \\ \bar{\Upsilon} &:= 2 \frac{\partial \bar{\psi}}{\partial \bar{\mathbf{H}}_1} \bar{\mathbf{H}}_1 + 2 \frac{\partial \bar{\psi}}{\partial \bar{\mathbf{H}}_2} \bar{\mathbf{H}}_2 \\ \mathbf{G}_1 &:= \mathbf{U}_g \frac{\partial \bar{\psi}}{\partial \bar{\mathbf{H}}_1} \mathbf{U}_g \\ \mathbf{G}_2 &:= \mathbf{U}_g \frac{\partial \bar{\psi}}{\partial \bar{\mathbf{H}}_2} \mathbf{U}_g, \end{aligned} \tag{A.2}$$

one obtains a compact form of the dissipation inequality in the form as in Eq. 45. Substitution of the prescribed form of \mathbf{U}_g , i.e.,

$$\mathbf{U}_g := \mathbf{I} + (\vartheta - 1) \boldsymbol{\gamma} \otimes \boldsymbol{\gamma}, \tag{A.3}$$

in the definition of $\bar{\mathbf{L}}_g$ (Eq. 40) shall then lead to

$$\bar{\mathbf{L}}_g = \left(\frac{\dot{\vartheta}}{\vartheta} \right) \boldsymbol{\gamma} \otimes \boldsymbol{\gamma}, \tag{A.4}$$

wherein

$$\mathbf{U}_g^{-1} = \mathbf{I} - \left(\frac{\vartheta - 1}{\vartheta} \right) \boldsymbol{\gamma} \otimes \boldsymbol{\gamma} \tag{A.5}$$

is utilized. It can additionally be shown that with such a choice for \mathbf{U}_g as in Eq. A.3,

$$\bar{\mathbf{H}}_i = \mathbf{U}_g \mathbf{H}_i \mathbf{U}_g = \mathbf{H}_i, \quad i = 1, 2. \tag{A.6}$$

With the help of Eqs. A.2 and A.4, and the fact that the growth direction $\boldsymbol{\gamma}$ is orthogonal to \boldsymbol{a}_{01} and \boldsymbol{a}_{02} that leads to $\bar{\boldsymbol{L}}_g \boldsymbol{H}_1 = \bar{\boldsymbol{L}}_g \boldsymbol{H}_2 = \mathbf{0}$, it can be shown that $\bar{\boldsymbol{\Upsilon}} : \bar{\boldsymbol{L}}_g = 0$. Hence, the dissipation inequality is further reduced from Eq. 45 to the form shown in Eq. 50.

Appendix B. Declarations

Appendix B.1. Funding

This work has been funded through the financial support of German Research Foundation (DFG) for the following projects:

1. “Drug-eluting coronary stents in stenosed arteries: medical investigation and computational modelling” (project number 395712048: RE 1057/44-1, RE 1057/44-2).
2. “In-stent restenosis in coronary arteries - in silico investigations based on patient-specific data and meta modeling” (project number 465213526: RE 1057/53-1), a subproject of “SPP 2311: Robust coupling of continuum-biomechanical in silico models to establish active biological system models for later use in clinical applications - Co-design of modeling, numerics and usability”.
3. “Modelling of Structure and Fluid-Structure Interaction during Tissue Maturation in Biohybrid Heart Valves”, a subproject of “PAK961 - Modeling of the structure and fluid–structure interaction of biohybrid heart valves on tissue maturation” (project number 403471716: RE 1057/45-1, RE 1057/45-2).

This is gratefully acknowledged.

Appendix B.2. Conflict of interest

The authors certify that they have no affiliations with or involvement in any organization or entity with any financial interest (such as honoraria; educational grants; participation in speakers’ bureaus; membership, employment, consultancies, stock ownership, or other equity interest; and expert testimony or patent-licensing arrangements), or non-financial interest (such as personal or professional relationships, affiliations, knowledge or beliefs) in the subject matter or materials discussed in this manuscript.

Appendix B.3. Availability of data

The data generated through the course of this work is stored redundantly and will be made available on demand.

Appendix B.4. Code availability

The custom-written routines will be made available on an open platform. The software package FEAP is proprietary and can therefore not be made available.

Appendix B.5. Contributions from the authors

K. Manjunatha determined the state of the art by reviewing relevant literature, set up governing differential equations, created the user subroutines for implementation in FEAP, interpreted the results, and wrote this article. K. Manjunatha and S. Reese developed the continuum theoretical framework contained within this work. N. Schaaps provided the microscopic and histological data that assisted the mathematical modeling process. M. Behr and F. Vogt participated in project discussions, provided conceptual advice, gave feedback on the interpretation of results, read the article, and provided valuable suggestions for improvement. All the authors approve the publication of this manuscript.

References

- [1] Dario Buccheri, Davide Piraino, Giuseppe Andolina, and Bernardo Cortese. Understanding and managing in-stent restenosis: a review of clinical data, from pathogenesis to treatment. *Journal of Thoracic Disease*, 8(10), 2016. ISSN 2077-6624. URL <https://jtd.amegroups.com/article/view/10071>.
- [2] D. Evans, Patricia V. Lawford, Julian P Gunn, Dawn C. Walker, D. Rodney Hose, Rod H. Smallwood, Bastien Chopard, Manfred Krafczyk, Jörg Bernsdorf, and Alfons G. Hoekstra. The application of multiscale modelling to the process of development and prevention of stenosis in a stented coronary artery. *Philosophical Transactions of the Royal Society A: Mathematical, Physical and Engineering Sciences*, 366:3343 – 3360, 2008.
- [3] Hannan Tahir, Alfons G. Hoekstra, Eric Lorenz, Patricia V. Lawford, D. Rodney Hose, Julian Gunn, and David J.W. Evans. Multi-scale simulations of the dynamics of in-stent restenosis: impact of stent deployment and design. *Interface Focus*, 1(3):365–373, 2011. doi: 10.1098/rsfs.2010.0024.
- [4] Hannan Tahir, Carles Bona-Casas, and Alfons G. Hoekstra. Modelling the effect of a functional endothelium on the development of in-stent restenosis. *PLoS ONE*, 8, 2013.
- [5] Hannan Tahir, Carles Bona-Casas, Andrew J. Narracott, Javaid Iqbal, Julian P Gunn, Patricia V. Lawford, and Alfons G. Hoekstra. Endothelial repair process and its relevance to longitudinal neointimal tissue patterns: comparing histology with in silico modelling. *Journal of The Royal Society Interface*, 11, 2014.
- [6] Hannan Tahir, Ioana Niculescu, Carles Bona-Casas, Roeland M. H. Merks, and Alfons G. Hoekstra. An in silico study on the role of smooth muscle cell migration in neointimal formation after coronary stenting. *Journal of The Royal Society Interface*, 12, 2015.
- [7] Colin J. Boyle, Alex B. Lennon, Michael Early, Daniel J. Kelly, Caitríona Lally, and Patrick J. Prendergast. Computational simulation methodologies for mechanobiological modelling: a

cell-centred approach to neointima development in stents. *Philosophical transactions. Series A, Mathematical, physical, and engineering sciences*, 368:2919 – 2935, 2010.

- [8] Colin J. Boyle, Alex B. Lennon, and Patrick J. Prendergast. In silico prediction of the mechanobiological response of arterial tissue: application to angioplasty and stenting. *Journal of biomechanical engineering*, 133 8:081001, 2011.
- [9] H. Zahedmanesh, H. Oosterwyck, and C. Lally. A multi-scale mechanobiological model of in-stent restenosis: deciphering the role of matrix metalloproteinase and extracellular matrix changes. *Computer Methods in Biomechanics and Biomedical Engineering*, 17(8):813–828, 2012. doi: 10.1080/10255842.2012.716830.
- [10] Houman Zahedmanesh, Hans Van Oosterwyck, and Caitríona Lally. A multi-scale mechanobiological model of in-stent restenosis: deciphering the role of matrix metalloproteinase and extracellular matrix changes. *Computer Methods in Biomechanics and Biomedical Engineering*, 17:813 – 828, 2014.
- [11] Maziyar Keshavarzian, Clark A. Meyer, and Heather N. Hayenga. Mechanobiological model of arterial growth and remodeling. *Biomechanics and Modeling in Mechanobiology*, 17:87–101, 2018.
- [12] Shibo Li, Long Lei, Ying Hu, Yanfang Zhang, Shijia Zhao, and Jianwei Zhang. A fully coupled framework for in silico investigation of in-stent restenosis. *Computer Methods in Biomechanics and Biomedical Engineering*, 22:217 – 228, 2018.
- [13] David R. Nolan and Caitríona Lally. An investigation of damage mechanisms in mechanobiological models of in-stent restenosis. *J. Comput. Sci.*, 24:132–142, 2018.
- [14] Pavel S. Zun, Tatiana Anikina, Andrew I. Svitenkov, and Alfons G. Hoekstra. A comparison of fully-coupled 3d in-stent restenosis simulations to in-vivo data. *Frontiers in Physiology*, 8, 2017.
- [15] Pavel S. Zun, Andrew J. Narracott, Claudio Chiastra, Julian P Gunn, and Alfons G. Hoekstra. Location-specific comparison between a 3d in-stent restenosis model and micro-ct and histology data from porcine in vivo experiments. *Cardiovascular Engineering and Technology*, 10:568 – 582, 2019.
- [16] Anna Corti, Monika Colombo, Francesco Migliavacca, José Félix Rodríguez Matas, Stefano Casarin, and Claudio Chiastra. Multiscale computational modeling of vascular adaptation: A systems biology approach using agent-based models. *Frontiers in Bioengineering and Biotechnology*, 9, 2021.

- [17] B. Fereidoon nezhad, R. Naghdabadi, S Sohrabpour, and G. A. Holzapfel. A mechanobiological model for damage-induced growth in arterial tissue with application to in-stent restenosis. *Journal of the Mechanics and Physics of Solids*, 101:311–327, 2017. doi: 10.1016/j.jmps.2017.01.016.
- [18] Ran He, Liguang Zhao, Vadim V. Silberschmidt, and Yang Liu. Mechanistic evaluation of long-term in-stent restenosis based on models of tissue damage and growth. *Biomechanics and Modeling in Mechanobiology*, 19:1425–1446, 2020. doi: 10.1007/s10237-019-01279-2.
- [19] Javier Escuer, Miguel A. Martínez, Sean McGinty, and Estefanía Peña. Mathematical modelling of the restenosis process after stent implantation. *Journal of the Royal Society Interface*, 16(157):20190313, 2019. doi: 10.1098/rsif.2019.0313.
- [20] Krishna C. Garikipati, Ellen M. Arruda, Karl Grosh, Harish Narayanan, and Sarah Calve. A continuum treatment of growth in biological tissue: the coupling of mass transport and mechanics. *Journal of The Mechanics and Physics of Solids*, 52:1595–1625, 2004.
- [21] Kiran Manjunatha, Marek Behr, Felix Vogt, and Stefanie Reese. A multiphysics modeling approach for in-stent restenosis: Theoretical aspects and finite element implementation. *Computers in Biology and Medicine*, 150:106166, 2022. ISSN 0010-4825. doi: <https://doi.org/10.1016/j.compbimed.2022.106166>. URL <https://www.sciencedirect.com/science/article/pii/S0010482522008745>.
- [22] Alfonso Caiazzo, David Evans, Jean-Luc Falcone, Jan Hegewald, Eric Lorenz, B. Stahl, Dinan Wang, Jörg Bernsdorf, Bastien Chopard, Julian P Gunn, D. Rodney Hose, Manfred Krafczyk, Patricia V. Lawford, Rod H. Smallwood, Dawn C. Walker, and Alfons G. Hoekstra. A complex automata approach for in-stent restenosis: Two-dimensional multiscale modelling and simulations. *J. Comput. Sci.*, 2:9–17, 2011.
- [23] Filippo Rossi, Tommaso Casalini, E Raffa, Maurizio Masi, and Giuseppe Perale. Bioresorbable polymer coated drug eluting stent: a model study. *Molecular pharmaceuticals*, 9 7:1898–910, 2012.
- [24] Valentina Busini, Paolo Arosio, and Maurizio Masi. Mechanistic modelling of avascular tumor growth and pharmacokinetics influence—part i. *Chemical Engineering Science*, 62:1877–1886, 2007.
- [25] Alistair McQueen, Javier Escuer, André Fensterseifer Schmidt, Ankush Aggarwal, Simon Kennedy, Christopher McCormick, Keith Oldroyd, and Sean McGinty. An intricate interplay between stent drug dose and release rate dictates arterial restenosis. *Journal of Controlled Release*, 349:992–1008, 2022. ISSN 0168-3659. doi: <https://doi.org/10.1016/j.jconrel.2022.07.037>. URL <https://www.sciencedirect.com/science/article/pii/S0168365922004722>.

- [26] Anotida Madzvamuse and Andy H. W. Chung. The bulk-surface finite element method for reaction-diffusion systems on stationary volumes. *Finite Elements in Analysis and Design*, 108:9–21, 2016.
- [27] Jordan S. Pober and William C. Sessa. Evolving functions of endothelial cells in inflammation. *Nature Reviews Immunology*, 7:803–815, 2007. doi: 10.1038/nri2171.
- [28] M Clozel, H Kuhn, F Hefti, and H R Baumgartner. Endothelial dysfunction and subendothelial monocyte macrophages in hypertension. effect of angiotensin converting enzyme inhibition. *Hypertension*, 18(2):132–141, 1991. doi: 10.1161/01.HYP.18.2.132.
- [29] H. J. S. Stewart, A. L. Guildford, D. J. Lawrence-Watt, and M. Santin. Substrate-induced phenotypical change of monocytes/macrophages into myofibroblast-like cells: A new insight into the mechanism of in-stent restenosis. *Journal of Biomedical Materials Research Part A*, 90A(2):465–471, 2009. doi: <https://doi.org/10.1002/jbm.a.32100>. URL <https://onlinelibrary.wiley.com/doi/abs/10.1002/jbm.a.32100>.
- [30] Frederick G.P. Welt and Campbell Rogers. Inflammation and restenosis in the stent era. *Arteriosclerosis, Thrombosis, and Vascular Biology*, 22(11):1769–1776, 2002. doi: 10.1161/01.ATV.0000037100.44766.5B.
- [31] Antonio Colombo and Giuseppe Sangiorgi. The monocyte: the key in the lock to reduce stent hyperplasia? **editorials published in the journal of the american college of cardiology reflect the views of the authors and do not necessarily represent the views of jaccor the american college of cardiology. *Journal of the American College of Cardiology*, 43(1):24–26, 2004. ISSN 0735-1097. doi: <https://doi.org/10.1016/j.jacc.2003.10.015>. URL <https://www.sciencedirect.com/science/article/pii/S0735109703013196>.
- [32] Steven O. Marx, Thottala Jayaraman, Loewe O. Go, and Andrew R. Marks. Rapamycin-fkbp inhibits cell cycle regulators of proliferation in vascular smooth muscle cells. *Circulation Research*, 76(3):412–417, 1995. doi: 10.1161/01.RES.76.3.412.
- [33] Amelia Barilli, Rossana Visigalli, Roberto Sala, Gian C. Gazzola, Alessandro Parolari, Elena Tremoli, Sabrina Bonomini, Alexandra Simon, Ellen I. Closs, Valeria Dall’Asta, and Ovidio Bussolati. In human endothelial cells rapamycin causes mTORC2 inhibition and impairs cell viability and function. *Cardiovascular Research*, 78(3):563–571, 02 2008. ISSN 0008-6363. doi: 10.1093/cvr/cvn024. URL <https://doi.org/10.1093/cvr/cvn024>.
- [34] Jan-Marcus Daniel, Jochen Dutzmann, Hannes Brunsch, Johann Bauersachs, Rüdiger Braun-Dullaeus, and Daniel G. Sedding. Systemic application of sirolimus prevents neointima formation not via a direct anti-proliferative effect but via its anti-inflammatory properties. *International Journal of Cardiology*, 238:79–91, 2017. ISSN 0167-5273. doi: <https://doi.org/10.1016/j.ijcard.2017.07.015>.

1016/j.ijcard.2017.03.052. URL <https://www.sciencedirect.com/science/article/pii/S016752731731611X>.

- [35] William T. Gerthoffer. Mechanisms of vascular smooth muscle cell migration. *Circulation Research*, 100:607–621, 2007. doi: 10.1161/01.RES.0000258492.96097.47.
- [36] Angus J. Grant, Nianji Yang, Matthew J. Moore, Yuen Ting Lam, Praveesuda L. Michael, Alex H.P. Chan, Miguel Santos, Jelena Rnjak-Kovacina, Richard P. Tan, and Steven G. Wise. Selective nlrp3 inflammasome inhibitor mcc950 suppresses inflammation and facilitates healing in vascular materials. *Advanced Science*, page 2300521, 2023. doi: <https://doi.org/10.1002/advs.202300521>. URL <https://onlinelibrary.wiley.com/doi/abs/10.1002/advs.202300521>.
- [37] Paula Budu-Grajdeanu, Richard C. Schugart, Avner Friedman, Christopher Valentine, Anil K. Agarwal, and Brad H. Rovin. A mathematical model of venous neointimal hyperplasia formation. *Theoretical Biology and Medical Modelling*, 5, 2008. doi: 10.1186/1742-4682-5-2.
- [38] M. Cilla, E. Penã, and M. Á. Martiné. Mathematical modelling of atheroma plaque formation and development in coronary arteries. *Journal of the Royal Society Interface*, 11:20130866, 2014. doi: 10.1098/rsif.2013.0866.
- [39] P. Sáez, E. Penã, M. A. Martínéz, and E. Kuhl. Mathematical modeling of collagen turnover in biological tissue. *Journal of Mathematical Biology*, 67:1765–1793, 2013. doi: 10.1007/s00285-012-0613-y.
- [40] Sean McGinty and Giuseppe Pontrelli. A general model of coupled drug release and tissue absorption for drug delivery devices. *Journal of Controlled Release*, 217:327–336, 2015. ISSN 0168-3659. doi: <https://doi.org/10.1016/j.jconrel.2015.09.025>. URL <https://www.sciencedirect.com/science/article/pii/S0168365915301267>.
- [41] Swapnil Salvi, Ankur Jain, Giuseppe Pontrelli, and Sean McGinty. Modeling dual drug delivery from eluting stents: The influence of non-linear binding competition and non-uniform drug loading. *Pharmaceutical Research*, 40:215–230, 2022. doi: <https://doi.org/10.1007/s11095-022-03419-3>.
- [42] Noriyuki Koyama, Charles E. Hart, and Alexander W. Clowes. Different functions of the platelet-derived growth factor- α and - β receptors for the migration and proliferation of cultured baboon smooth muscle cells. *Circulation Research*, 75(4):682–691, 1994. doi: 10.1161/01.res.75.4.682.
- [43] Tom J. Parry, Rathna Thyagarajan, Dennis Argentieri, Robert Falotico, John Siekierka, and Ronald J. Tallarida. Effects of drug combinations on smooth muscle cell proliferation: An

- isobolographic analysis. *European Journal of Pharmacology*, 532(1):38–43, 2006. ISSN 0014-2999. doi: <https://doi.org/10.1016/j.ejphar.2005.12.042>. URL <https://www.sciencedirect.com/science/article/pii/S001429990501352X>.
- [44] Lucia Napione, Simona Pavan, Andrea Veglio, Andrea Picco, Guido Boffetta, Antonio Celani, Giorgio Seano, Luca Primo, Andrea Gamba, and Federico Bussolino. Unraveling the influence of endothelial cell density on VEGF-A signaling. *Blood*, 119(23):5599–5607, 06 2012. ISSN 0006-4971. doi: 10.1182/blood-2011-11-390666. URL <https://doi.org/10.1182/blood-2011-11-390666>.
- [45] Tom J. Parry, Ruth Brosius, Rathna Thyagarajan, Demetrius Carter, Dennis Argentieri, Robert Falotico, and John Siekierka. Drug-eluting stents: Sirolimus and paclitaxel differentially affect cultured cells and injured arteries. *European Journal of Pharmacology*, 524(1):19–29, 2005. ISSN 0014-2999. doi: <https://doi.org/10.1016/j.ejphar.2005.09.042>. URL <https://www.sciencedirect.com/science/article/pii/S0014299905009064>.
- [46] E. K. Rodriguez, A Hoger, and A. D. McCulloch. Stress-dependent finite growth in soft elastic tissues. *Journal of Biomechanics*, 27(4):455–467, 1994. doi: 10.1016/0021-9290(94)90021-3.
- [47] Bob Svendsen. A thermodynamic formulation of finite-deformation elastoplasticity with hardening based on the concept of material isomorphism. *International Journal of Plasticity*, 14(6):473–488, 1998. ISSN 0749-6419. doi: [https://doi.org/10.1016/S0749-6419\(98\)00002-3](https://doi.org/10.1016/S0749-6419(98)00002-3). URL <https://www.sciencedirect.com/science/article/pii/S0749641998000023>.
- [48] S. Reese, T. Brepols, M. Fassin, L. Poggenpohl, and S. Wulfinghoff. Using structural tensors for inelastic material modeling in the finite strain regime – a novel approach to anisotropic damage. *Journal of the Mechanics and Physics of Solids*, 146:104174, 2021. doi: 10.1016/j.jmps.2020.104174.
- [49] Hagen Holthusen, Christiane Rothkranz, Lukas Lamm, Tim Brepols, and Stefanie Reese. Inelastic material formulations based on a co-rotated intermediate configuration—application to bioengineered tissues. *Journal of the Mechanics and Physics of Solids*, 172:105174, 2023. ISSN 0022-5096. doi: <https://doi.org/10.1016/j.jmps.2022.105174>. URL <https://www.sciencedirect.com/science/article/pii/S0022509622003507>.
- [50] Ellen Kuhl and Paul Steinmann. Theory and numerics of geometrically non-linear open system mechanics. *International Journal for Numerical Methods in Engineering*, 58:1593–1615, 2003.
- [51] B. Coleman and W. Noll. The thermodynamics of elastic materials with heat conduction and viscosity. *Archive for Rational Mechanics and Analysis*, 13:167–178, 1963. doi: 10.1007/BF01262690.

- [52] Vlado A Lubarda and Anne Hoger. On the mechanics of solids with a growing mass. *International Journal of Solids and Structures*, 39:4627–4664, 2002.
- [53] L. Lamm, H. Holthusen, T. Brepols, S. Jockenhövel, and S. Reese. A macroscopic approach for stress driven anisotropic growth in bioengineered soft tissues. *Biomechanics and Modeling in Mechanobiology*, 21:627–645, 2022. doi: <https://doi.org/10.1007/s10237-021-01554-1>.
- [54] G. A. Holzapfel, Thomas C. Gasser, and Ray W. Ogden. A new constitutive framework for arterial wall mechanics and a comparative study of material models. *Journal of elasticity and the physical science of solids volume*, 61:1–48, 2000. doi: 10.1023/A:1010835316564.
- [55] J. Korelc. Multi-language and multi-environment generation of nonlinear finite element codes. *Engineering with Computers*, 18:312–327, 2002. doi: 10.1007/s003660200028.
- [56] J. Korelc. Automation of primal and sensitivity analysis of transient coupled problems. *Computational Mechanics*, 44:631–649, 2009. doi: 10.1007/s00466-009-0395-2.
- [57] Christie Alappat, Achim Basermann, Alan R. Bishop, Holger Fehske, Georg Hager, Olaf Schenk, Jonas Thies, and Gerhard Wellein. A recursive algebraic coloring technique for hardware-efficient symmetric sparse matrix-vector multiplication. *ACM Trans. Parallel Comput.*, 7(3), June 2020. ISSN 2329-4949. doi: 10.1145/3399732. URL <https://doi.org/10.1145/3399732>.
- [58] Matthias Bollhöfer, Olaf Schenk, Radim Janalik, Steve Hamm, and Kiran Gullapalli. *State-of-the-Art Sparse Direct Solvers*. Springer International Publishing, Cham, 2020. ISBN 978-3-030-43736-7. doi: 10.1007/978-3-030-43736-7_1. URL https://doi.org/10.1007/978-3-030-43736-7_1.
- [59] Matthias Bollhöfer, Aryan Eftekhar, Simon Scheidegger, and Olaf Schenk. Large-scale sparse inverse covariance matrix estimation. *SIAM Journal on Scientific Computing*, 41(1):A380–A401, 2019. doi: 10.1137/17M1147615. URL <https://doi.org/10.1137/17M1147615>.
- [60] Meike Gierig, Peter Wriggers, and Michele Marino. Arterial tissues and their inflammatory response to collagen damage: A continuum in silico model coupling nonlinear mechanics, molecular pathways, and cell behavior. *Computers in Biology and Medicine*, 158:106811, 2023. ISSN 0010-4825. doi: <https://doi.org/10.1016/j.compbimed.2023.106811>.